DETERMINING SPECULAR, DIFFUSE, AND AMBIENT COLOR

MATERIAL PROPERTIES OF INDUSTRIAL

PLANT PRIMITIVES

by

Brandon James Baker

A dissertation submitted to the faculty of
The University of Utah
in partial fulfillment of the requirements for the degree of

Doctor of Philosophy

Department of Electrical and Computer Engineering

The University of Utah

May 2014

The University of Utah Graduate School

STATEMENT OF DISSERTATION APPROVAL

The dissertation of **Brandon James Baker**

has been approved by the following supervisory committee members:

Cynthia M. Furse	, Chair	**1/2/2014**
		Date Approved
J. Mark Baird	, Member	**1/2/2014**
		Date Approved
Robert Palais	, Member	**1/2/2014**
		Date Approved
Rong Rong Chen	, Member	**1/2/2014**
		Date Approved
Michael Zhdanov	, Member	**1/2/2014**
		Date Approved

and by **Gianluca Lazzi** , Chair of

the Department of **Electrical and Computer Engineering**

and by David B. Kieda, Dean of The Graduate School.

ABSTRACT

Three-dimensional (3D) models of industrial plant primitives are used extensively in modern asset design, management, and visualization systems. Such systems allow users to efficiently perform tasks in Computer Aided Design (CAD), life-cycle management, construction progress monitoring, virtual reality training, marketing walk-throughs, or other visualization. Thus, capturing industrial plant models has correspondingly become a rapidly growing industry. The purpose of this research was to demonstrate an efficient way to ascertain physical model parameters of reflectance properties of industrial plant primitives for use in CAD and 3D modeling visualization systems.

The first part of this research outlines the sources of error corresponding to 3D models created from Light Detection and Ranging (LiDAR) point clouds. Fourier analysis exposes the error due to a LiDAR system's finite sampling rate. Taylor expansion illustrates the errors associated with linearization due to flat polygonal surfaces. Finally, a statistical analysis of the error associated with LiDAR scanner hardware is presented.

The second part of this research demonstrates a method for determining Phong specular and Oren-Nayar diffuse reflectance parameters for modeling and rendering pipes, the most ubiquitous form of industrial plant primitives. For specular reflectance, the Phong model is used. Estimates of specular and diffuse parameters of two ideal

cylinders and one measured cylinder using brightness data acquired from a LiDAR scanner are presented. The estimated reflectance model of the measured cylinder has a mean relative error of 2.88% and a standard deviation of relative error of 4.0%.

The final part of this research describes a method for determining specular, diffuse and color material properties and applies the method to seven pipes from an industrial plant. The colorless specular and diffuse properties were estimated by numerically inverting LiDAR brightness data. The color ambient and diffuse properties are estimated using k-means clustering. The colorless properties yielded estimated brightness values that are within an RMS of 3.4%, with a maximum of 7.0% and a minimum of 1.6%. The estimated color properties effected an RMS residual of 13.2% with a maximum of 20.3% and a minimum of 9.1%.

I dedicate this dissertation to my wife, Melanie and to my children, Isaac, Benjamin,

Lilia, William Joseph and Amelia.

TABLE OF CONTENTS

Chapter

LIST OF TABLES

LIST OF FIGURES

ACKNOWLEDGMENTS

CHAPTER 1

INTRODUCTION

1.1   The Need for 3D Models of Industrial Plants

Three-dimensional (3D) models of industrial plant primitives are used extensively

in modern asset design, management, and visualization systems. Such systems allow

users to efficiently perform tasks in Computer Aided Design (CAD), life-cycle

management, plant inspection, construction progress monitoring, virtual reality training,

marketing walk-throughs, or other visualization. From oil and gas, hydroelectric or

nuclear power, to food and goods manufacturing, industrial plants are an ever-growing

aspect of modern society. Virtual reality training systems, for example, rely on visually

and geometrically accurate 3D models to provide realistic immersive environments to

prepare individuals for emergency situations [1]-[4]. Marketing walk-throughs also

provide a much more compelling effect when the visual aspect is of the highest quality

[5]-[7]. Thus, capturing, annotating, and visualizing industrial plants has correspondingly

become a rapidly growing industry and an increasingly important aspect of research.

"As-builts" are databases containing existing condition information about a

human architected structure. Ascertaining as-built information for industrial plants

usually involves taking measurements, utilizing those measurements to create geometric

primitives (such as pipes, flanges, elbows etc.), annotating those primitives with

descriptive information, and storing the results in a database for future use. Such annotation information may include: color, material type, outer diameter, inner diameter, material density, melting point, specific heat, purchase price, purchase date, the current condition the material is in, or even its life expectancy.

Light Detection and Ranging (LiDAR) scanners are frequently used to capture 3D points and color photographic data of industrial plants. Such data contain vast amounts of information that is scarcely utilized to its full potential. For example, the visual aspect of the as-built information (if even available in a useful format) is underutilized in most circumstances [8]. Although many applications today can render massive amounts of 3D points (called "point clouds"), these systems do not exceed the visual quality of a polygonal 3D model, especially given the extreme capabilities of modern graphics hardware. Hence, point clouds are typically used to display and work with raw data, but not the final model.

An alternative to point clouds is photorealistic texture-based CAD rendering systems [9] [10]. These systems excel in visual quality, yet are not as widespread and still require powerful rendering graphics hardware to operate and require large amounts of storage space in RAM and on a computer's hard drive. Point cloud and other texture-based rendering systems typically rely heavily on level of detail (LOD) engines to page points in and out of the rendering buffer. Even the world's best graphics systems present artifacts when paging data in and out of the graphics hardware, causing visual artifacts, and heavy power usage. In fact, even with widespread availability of powerful graphics hardware, few existing computer aided design (CAD) visualization and utilization tools are even programmed to properly render photorealistic textures and material properties of

3D CAD models [8].

<div align="center">

1.2   <u>Contributions</u>

</div>

The purpose of this research is to offer an efficient alternative to point clouds or texture mapping to achieve near photorealistic rendering with minimal storage for 3D models of industrial plant primitives. First, geometric models of pipes were created. Colorless specular and diffuse material properties were then estimated using LiDAR intensity data. Finally, colored ambient and diffuse material properties were determined and combined with the colorless specular and diffuse materials to create models that require very little digital storage resources and can be rendered efficiently on common graphics hardware.

<div align="center">

1.2.1   Geometric Modeling from 3D Spatial Data

</div>

Effectively modeling the geometry of an industrial plant primitive is the first step in obtaining material properties of a model. Understanding the errors associated with 3D model geometries created from LiDAR data helps minimize errors estimated for material properties. To this end, an error analysis of modeling LiDAR data from terrestrial scanners is presented in this project. When a particular application requires additional accuracy, the solution typically involves scanning at a higher resolution of 3D spatial data. This reliance on data directly acquired from LiDAR scanners has forced many users to gather redundant data at the expense of efficiency. This paper explores the sources of error associated with LiDAR data and the effects of ray tracing polygonal LiDAR data as an alternate to acquiring and utilizing high density scans. The errors are

quantified for a paved surface; however, the results may be applied to many other types of surfaces. The results of this analysis demonstrate that polygonal models of terrestrial LiDAR data are accurate methods for representing Digital Terrain Models (DTMs). The results further demonstrate that the accuracy of a polygon created from LiDAR data can be higher than scanning at a higher resolution for many applications.

1.2.2   Colorless Specular and Diffuse Properties

Specular reflectance is the modeling of light as it reflects off a surface at a single (or very limited number of) angle(s).   Specular reflectance describes an object's "shininess." Diffuse reflectance is the reflectance of light that scatters in many angles, is not "shiny," and is largely responsible for illustrating the contrast between brightness and darkness of the colors we see in objects.   The methods presented in this project automatically extract colorless specular and diffuse material properties from raw LiDAR data of pipes found in industrial plants.   These colorless quantities can be utilized to create life-like visual lighting effects on readily available graphics hardware, given the proper rendering engine.

1.2.3   Colored Ambient, Diffuse, and Specular Properties

Ambient reflectance is a quantity commonly used in computer graphics systems to efficiently portray the color of an object or portion of an object that lacks direct illumination. The three quantities of ambient, diffuse, and specular color information, when utilized properly in a rendering engine, can provide a near photorealistic visual experience for a user of a CAD system, an asset management tool, a customer, or a

trainee. This project presents a method for combining the colorless diffuse and specular material properties previously determined with colored photographic data to estimate colored specular, diffuse, and ambient material properties of industrial plant primitives.

1.3   Material Property Estimation Experimental Setup

This project utilized two types of measurement data acquired in an industrial plant. The first type was color image data from a digital camera found inside the LiDAR scanner. The second type was range, azimuth, polar, and intensity data acquired from a (Light Detection and Ranging) LiDAR scanner. The color image data consisted of red, green, and blue arrays of detected light in the visible spectrum. The LiDAR data partially consisted of range, azimuth, and polar three-dimensional spatial data that were used to fit pipes to the measured points. The range, azimuth, and polar data are simply the three values that uniquely determine location in three dimensions in spherical coordinates and can be easily converted to x, y, and z values in Cartesian coordinates.

Intensity data were also acquired and utilized using the LiDAR scanner. This intensity value for each measured 3D point represents the reflectance value (ratio) between the transmitted and received brightness of the near-infrared LiDAR source. Figure 1-1 , Figure 1-2, and Figure 1-3 are the color image, intensity image, and intensity image with labels marking the seven pipes that were analyzed for this project, respectively.

Pipe number 2 shown in Figure 1-3 is the same pipe analyzed in Chapter 4. The results of the estimation of the color material properties for the seven pipes are found in Chapter 5.

The LiDAR scanner was stationed on a tripod and a 360 degree (horizontally) scan was performed. The color camera is integrated with the LiDAR scanner, thus, each 3D point acquired by the LiDAR scanner has a red, green, blue, and LiDAR intensity value associated with it.

1.4   Summary

This dissertation offers an efficient alternative to point clouds or texture mapping to achieve near photorealistic rendering and minimal storage for 3D models of industrial plant primitives. First, it provides a detailed explanation of the sources of error associated with 3D models made from LiDAR scan data. Next, it describes a method for extracting colorless specular and diffuse reflectance parameters for industrial plant primitives. Then, a method for determining color material properties is presented.

A detailed description of the format of this dissertation follows:

Chapter 2 outlines the current state of the art of this field of research.

Chapter 3 describes a numerical analysis of the sources of errors associated with 3D modeling of planar surfaces from LiDAR scan data.

Chapter 4 provides a method for determining colorless specular and diffuse material properties from LiDAR intensity data. In Section 4.2, more details regarding related work found in the literature is presented. Section 4.3 outlines some details of industrial plant modeling of cylindrical objects such as pipes, railings, supports, etc., where the specific mathematical representations of specular and diffuse reflectance models are provided and described. Section 4.3.1 illustrates the difference between the Oren-Nayar and Lambertian diffuse reflectance models.

The numerical inversion process used in this paper is described in Section 4.4. The experimental results are outlined in Section 4.5.

Chapter 5 applies the method described in Chapter 4 to seven pipes in an industrial plant and then offers a method for determining ambient and diffuse color information from digital photographic data.

The methods outlined in Section 5.2 are divided into two parts. Section 5.2.1 describes several case studies of the specular and diffuse estimation method proposed in [11] applied to measurement data from seven different pipes found in an industrial plant. LiDAR scan intensity (brightness) data are used to estimate the specular and diffuse material properties. Section 5.2.2 offers a k-means color determination method applied to the same seven pipes. Digital photographic data of the pipes are used to estimate the ambient and diffuse colors. Section 5.3, which is also divided into two parts, offers the results and corresponding discussion of the estimations. Section 5.3.1 presents and describes the results for the colorless specular and diffuse estimation, and Section 5.3.2 presents and describes the results of the ambient and diffuse color estimations. Concluding remarks for this chapter are provided in Section 5.4.

1.5   Publications

The work in this paper has been published in IEEE Geoscience and Remote Sensing Symposium in 2008 in Boston [12]; [11] has been submitted for publication in "Geometry, Imaging and Computing" and the content in Chapter 5 will soon be submitted to "Automation in Construction" for publication.

1.6   References

[1]   Rabbani Shah, T., "Automatic reconstruction of industrial installations using point clouds and images." Ph.D. dissertation, Dept. Elect. Eng., Delft Univ. of Tech., Delft, Netherlands.

[2]   Jorge, C., et al. (2010, Aug 17) *Nuclear Plants and Emergency Virtual Simulations Based on a Low-Cost Engine Reuse. Nuclear Power*, [Online]. Available: http://www.intechopen.com/books/ nuclear-power/nuclear-plants-and-emergency-virtual-simulations-based-on-a-low-cost-engine-reuse

[3]   Cook, J., "Virtual Reality for large-scale industrial applications," *Future Generation Computer Systems*, vol 14, Issue 3-4, August 1998, pp. 157-166

[4]   Hubbold, R., "The Use of Virtual Reality for Training Process Plant Operatives", *Computer Graphics Expo '94 Conference*, Wembley, London, 9th November 1994.

[5]   Manocha, D. "Interactive Walkthroughs of Large Geometric Datasets," *SIGGRAPH 1999*, Los Angeles, CA, USA, 1999.

[6]   Hubbold, R., "Landmarking for navigation of large models," *Computers and Graphics*, vol. 23, no. 5, pp. 729-738, 1999.

[7]   Aliaga, D., "A Framework for the Real-time Walkthrough of Massive Models," UNC Chapel Hill, Comp. Sci. Technical Report, TR98-013, 1998.

[8]   Toro, C., "Improving Virtual reality Applications in CAD through Semantics," *The International Journal of Virtual Reality*, vol. 5, no. 4, pp 39-46., Apr 1996.

[9]   Calabi Yau Systems. (2013, Dec 26), *LD3 Studio*, http://www.calabiyausystems .com/ Products-LD3Studio.aspx#!/page_products_ld3studio

[10]   Bentley Systems Website, (2013, Dec 12), *Microstation Productline*. [Online]. http://www.bentley.com/en-US/Products/microstation+product+line/

[11]   Baker, B., Furse, C., "Determining Reflectance Properties of Industrial Plant Primitives," submitted to: Geometry, Imaging and Computing, 2013

[12]   Baker, B., "IEEE Geoscience and Remote Sensing Symposium Journal, 2008", Boston, MA, July 6-11, 2008, pp 257-260.

Figure 1-1 Measured color image data acquired by a digital camera embedded in the LiDAR scanner

Figure 1-2 Measured brightness data acquired by a LiDAR scanner
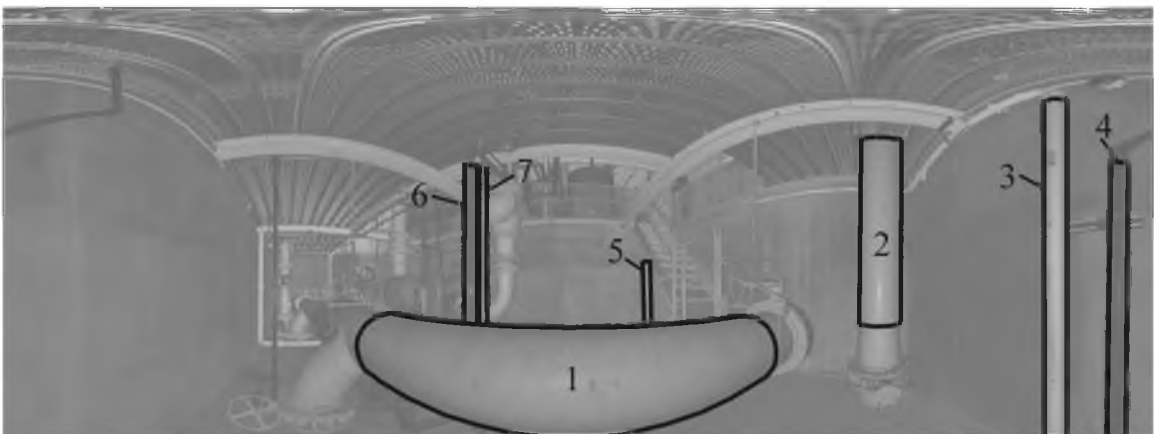
Figure 1-3 Measured brightness data with pipes that were analyzed and numbered

CHAPTER 2

3D MODELING AND VISUALIZATION OF INDUSTRIAL

PLANT PRIMITIVES

2.1   The Current State of the Art of 3D Modeling Industrial Plant Primitives

3D model material properties are difficult to attain yet can be used extensively for visualization in computer graphics systems. Such visualization systems are used in Computer Aided Design (CAD) and inspection [1],[2], virtual reality training [3]-[6], and marketing or other walk-through [7]-[9] applications. Automated or semi-automated CAD model generation from industrial plants is a growing area of research and development. Methods used include photogrammetry [10],[11], Light Detection and Ranging (LiDAR) laser scanning [12]-[16], or both [17],[3]. Other applications of 3D model material properties may include automated object recognition, construction progress tracking [19], or object condition assessment [20].

These methods for modeling industrial plant primitives in the literature focus on determining the objects' geometry – size of pipe, orientation in space, its clearance from other objects, etc. This project uses LIDAR data similar to [14] and [17], but we automatically determine colored ambient, diffuse, and specular reflectance properties instead of primitive geometry.

2.2   Error Analysis of 3D Modeling from LiDAR Data

Many researchers have performed error analyses on various algorithms that process aerial LiDAR scanning data [21]-[28]. In [21], the authors analyze various algorithms used to estimate spatial data from LiDAR data to create DEMs and DTMs. These previous works describe observations of error in specific environments but do not provide a complete mathematical basis to address the reasons why the particular results were observed. Additional publications discuss the processing of airborne LiDAR data for DTM extraction [29]-[31]. [29] analyzes LiDAR data DTM extraction via adaptive processing; [30] discusses modeling of LiDAR waveforms in vegetation populated terrains; [31] offers insight into techniques for analyzing bathymetric LiDAR data. Chapter 3 of this paper explains the mathematics behind estimation theory as it applies to LiDAR scan data.   Section 3.4 analyzes the sources of error related to modeling polygonal models from LiDAR data. Chapter 3 also offers several illustrative examples of the errors associated with actual and modeled scan data to make an accurate assessment of the strengths and limitations of ray tracing on polygonal models.

2.3   Reflectance Material Properties of 3D Models

Properties of light as they interact with an object and are perceived by human eyes have been researched for centuries [32]-[35]. Lambert offered a basic mathematical model that describes this interaction, and the Lambertian model [32] is still the most prevalent algorithm for computing diffuse reflectance today. The Lambertian model calculates the brightness of a particular point on an object based on the object's inherent color, the reflected angle of the light source, and its relation to the angle of the viewing

direction. The visual properties of light, such as Lambertian reflectance, were applied to computer systems to enhance realism in computer graphics in the 1960s. Cook, Torrance, Sparrow, Phong, and Blinn contributed a great deal of pioneering work in the field [36]-[39]. The efficient approximation of specular reflectance is one aspect of early advances in computer graphics that has withstood the test of time.

2.3.1   Generalized Diffuse Reflectance

Oren and Nayar introduced a generalization of Lambert's solution to the diffuse reflectance model by accounting for rough surfaces that scatter light more prevalently than other relatively smooth surfaces [39]. This contribution, although not as computationally efficient as the Lambertian model, provides a much more accurate representation for rough surfaces. We utilize the Oren Nayar generalized model of diffuse reflectance as the model for our diffuse material property estimation. Chapter 4 offers a method for calculating the Oren Nayar diffuse material properties from LiDAR scan data.

2.3.2   Phong Specular Reflectance

Phong illustrated a method for calculating the bright reflective material property that shiny surfaces demonstrate [38]. We utilize the Phong model as the model for our specular material property estimation. In addition to estimating the Oren Nayar diffuse parameters, Chapter 4 also offers a method for calculating the Phong specular material properties from LiDAR scan data.

2.3.3   Applications of Light Reflectance Modeling

Applications utilizing diffuse and specular reflectance models have yielded advances in the field of determining the geometric properties of an object [40]-[59]. "Shape from shading," as it is more commonly called, has seen dramatic advances over the years.   Specular highlights, specifically, can provide detailed and accurate information regarding the detailed shape of a surface in addition to its reflective properties. Nayar et al. uses reflectance to perform object recognition [50].

The general science of specular and diffuse reflectance has seen significant attention.   Brelstaff et al. have utilized Lambertian constraints to detect specular reflection parameters [44]. Nayar et al. have published work relating the surface reflection parameters of a model to its physical and geometrical properties [48]. Soon thereafter, Nayar et al. contributed additional work outlining the identification and removal of specular highlights using color and polarization [60]. Wolff, Nayar, and Oren then published work that applies their enhanced reflectance models for computer vision [56]. Lin and Lee provide several methods for enhancing the visual appearance of objects utilizing specular and diffuse properties [61]-[63]. Ragheb et al. illustrated a method for separating Lambertian and specular reflectance parameters for Machine Vision [64]. More recently, Nayar outlined a method for overcoming challenges in shape from shading techniques using a diffuse filter to alleviate specular highlights and shadowed regions common in digital images [65].

Chapter 5 of this paper describes how the theory proposed herein can be applied to real-world measurement data of industrial plant pipes. Additionally, a method for determining color information is also provided in that chapter.

2.4   Rendering 3D Models of Industrial Plant Primitives

Although most CAD systems render very simple visual information associated with the model, some systems can render photorealistic textures [66], [67]. Photorealistic models are visually appealing, yet they require large amounts of hard drive and RAM storage space, and are computationally intensive to visualize. Even level of detail (LOD) engines cannot operate efficiently without storing, paging, and purging massive amounts of detailed visual information in real-time. The material properties determined in this paper can be efficiently applied to real-time rendering systems due to minimal memory storage requirements and readily available graphics hardware.

2.5   Summary of the Current State of the Art

This paper describes a method for determining material properties of industrial plant primitives for visualization, design, object recognition, and other potential applications. Most research in the current state of the art for pipes in industrial plants focuses on fitting geometry only, while some applications apply bulky texture maps to the surface, but lack the physical descriptive data that characterize the objects' fundamental material properties. This paper acquires those fundamental data and demonstrates how they can be applied to enhance 3D modeling and design applications.

2.6   References

[1]   Posada, J., "Ontology Supported Semantic Simplification of Large Data Sets of Industrial Plant CAD Models for Design Review Visualization," *Knowledge-Based Intelligent Information and Engineering Systems*, vol. 46, no. 1-2, Jan 2005.

[2]   Roh, S., "Visualization Application for Interior Progress Monitoring. 3D Environment," *Construction Research Congress (CRC)*, Seattle, Washington, April 5-7, 2009.

[3]   Rabbani Shah, T., "Automatic reconstruction of industrial installations using point clouds and images." Ph.D. dissertation, Dept. Elect. Eng., Delft Univ. of Tech., Delft, Netherlands.

[4]   Jorge, C., et al. (2010, Aug 17) *Nuclear Plants and Emergency Virtual Simulations Based on a Low-Cost Engine Reuse. Nuclear Power*, [Online]. Available: http://www.intechopen.com/books/ nuclear-power/nuclear-plants-and-emergency-virtual-simulations-based-on-a-low-cost-engine-reuse

[5]   Cook, J., "Virtual Reality for large-scale industrial applications," *Future Generation Computer Systems*, vol 14, Issue 3-4, August 1998, pp. 157-166

[6]   Hubbold, R., "The Use of Virtual Reality for Training Process Plant Operatives", *Computer Graphics Expo '94 Conference*, Wembley, London, 9th November 1994.

[7]   Manocha, D. "Interactive Walkthroughs of Large Geometric Datasets," *SIGGRAPH 1999*, Los Angeles, CA, USA, 1999.

[8]   Hubbold, R., "Landmarking for navigation of large models," *Computers and Graphics*, vol. 23, no. 5, pp. 729-738, 1999.

[9]   Aliaga, D., "A Framework for the Real-time Walkthrough of Massive Models," UNC Chapel Hill, Comp. Sci. Technical Report, TR98-013, 1998.

[10]   Chapman, D., "An omnidirectional imaging system for the reverse engineering of industrial facilities," *The International Archives of the Photogrammetry, Remote Sensing and Spatial Information Sciences*, vol. 34, no. XXX, 8 pages, 2004.

[11]   Tangelder, J. W. H., "Cad-based photogrammetry for reverse engineering of industrial installation," *Computer-Aided Civil and Infrastructure Engineering*, vol. 18, no. 1, pp. 264–274, Jan 2003.

[12]   Tang, P., "Automatic reconstruction of as-built building information models from laser-scanned point clouds: A review of related techniques", *Automation in Construction*, Volume 19, Issue 7, Pages 829-843, November 2010.

[13]   Khalifa, I., "Range image segmentation using local approximation of scan lines with application to cad model acquisition," *Machine Vision Applications*, vol. 13, no.5-6, pp. 263–274, 2003.

[14]   Goulette. F. "Automatic CAD modeling of industrial pipes from range images," *Proc., Int. Conf on Recent Advances in 3- D Digital Imaging and Modeling,* Ottawa, Ontario, Canada, May 1997, pp. 229-233.

[15]   Sanders, F. H., "3D Laser Scanning Helps Chevron Revamp Platform," *Oil-and-Gas-Journal,* 2001.

[16]   Lee, J., "Skeleton-based 3D reconstruction of as-built pipelines from laser-scan data," *Automation in Construction.* vol.35, Nov 2013, pp 199–207.

[17]   Hong, J. "3D modelling of industrial piping systems using digital photogrammetry and laser scanning," M.S. Thesis, Dept. Elec. Eng., Ryerson Univ., Ottawa, Ontario, Canada, 2003.

[18]   Rabbani Shah, T., "Automatic reconstruction of industrial installations using point clouds and images." Ph.D. dissertation, Dept. Elect. Eng., Delft Univ. of Tech., Delft, Netherlands.

[19]   Turkan, Y., "Automated progress tracking using 4D schedule and 3D sensing technologies," *Automation in Construction,* vol. 22, March 2012, Pages 414-421.

[20]   Mohammad R. "Adaptive vision-based crack detection using 3D scene reconstruction for condition assessment of structures," *Automation in Construction,* vol. 22, March 2012, Pages 567-576.

[21]   Smith, S.L., "The importance of understanding error in lidar digital elevation models", *XXth ISPRS Congress,* Istanbul, Turkey, 2004.

[22]   Declercq, F.A.N "Interpolation methods for scattered sample data: Accuracy, spatial patterns, processing time," *Cartography and Geographical Information Systems,* vol. 23, no. 3, 1996, 128-144.

[23]   Desmet, P.J.J "Effects of interpolation errors on the analysis of DEMs," *Earth Surface Processes and Landforms,* vol. 22, 1997, pp. 128-144.

[24]   Maas, H.G. "Two Algorithms for Extracting Building Models from Raw Laser Altimetry Data," *ISPRS Journal of Photogrammetry and Remote Sensing,* vol. 54 1999, pp. 153-163.

[25]   Morgan, M, "Interpolation of LiDAR Data and Automative Building Extraction," ACSM-ASPRS 2002 Ann. Conf. Proc., Washington D.C., USA, 2002.

[26]   Rees, W.G., "The accuracy of Digital Elevation Models interpolated to higher resolutions," *International Journal of Remote Sensing,* vol. 21, no 1, 2000, pp. 7-20.

[27]   Sandwell, D. T., "Biharmonic Spline Interpolation of GEOS-3 and SEASAT Altimeter Data", *Geophysical Research Letters*, vol. 2, pp. 139-142, 1987.

[28]   Smith, S.L, "Interpreting Interpolation: The Pattern of Interpolation Errors in Digital Surface Models Derived from Laser Scanning Data," *Proceedings of GISRUK 2003*, London, England, 2003.

[29]   Hyun S. L., "DTM Extraction of Lidar Returns Via Adaptive Processing", *IEEE TGARS*, vol. 41, no. 9, Sept 2003.

[30]   Ni-Meister, W. "Modeling Lidar Waveforms in Heterogeneous and Discrete Canopies", *IEEE Transactions on Geoscience and Remote Sensing*, vol. 39, no. 9, Sept 2001.

[31]   Wong, H., "One-Dimensional Signal Processing Techniques for Airborne Laser Bathymetry," *IEEE TGARS*, vol. 32, no. 1, Jan 1994.

[32]   Lambert, J., "Photometria sive de mensure de gratibus luminis, colorum umbrae, " Leipzig, Germany, W. Engelmann, 1760.

[33]   Kerker, M., "The Scattering of Light," New York, Academic, 1909.

[34]   Mandelstam, L.I., "Light Scattering by Inhomogeneous Media," Zh. Russ. Fiz-Khim. Ova. Ch 58, pp 381, 1926.

[35]   Kubelka, P., „Ein Beitrag zur Optik der Farbanstriche," Zeits. f. Techn. Physik, 12, 593–601, 1931. (see The Kubelka-Munk Theory of Reflectance)

[36]   Blinn, J. "Models of light reflection for computer synthesized pictures," *Computer Graphics, SIGGRAPH '77 Proceedings*, 187, San Jose, CA, 1977.

[37]   Cook, R., "A reflectance model for computer graphics," *ACM Transactions on Graphics*, vol. 1, no. 1, Jan 1982, pp. 7-24.

[38]   Phong, B., "Illumination for Computer Generated Pictures," *Communications of the ACM*, vol. 18, no. 6, pp. 311-317, 1975.

[39]   Oren, M., „Generalization of the Lambertian model and implications for machine vision," *International Journal of Computer Vision*, vol. 14, no. 3, 1995, pp. 227-251.

[40]   Horn, B.K.P., "Determining Shape and Reflectance Using Multiple Images," *Massachussetts Institute of Technology*, 1978, pp. 113-115.

[41]   Koenderink, J.J., The Internal Representation of Solid Shape with Respect to Vision. Biological Cybernetics, vol. 32, 1979, pp. 211-216.

[42] Horn, B.K.P., "The Variational Approach to Shape from Shading," *Computer Vision, Graphics, and Image Processing*, vol. 33, no. 2, 1986, pp. 174-208.

[43] Healey, G.H., "Local Shape from Specularity," *IEEE International Conference on Computer Vision*, 1987, pp. 151-160.

[44] Brelstaff, G., "Detecting Specular Reflection Using Lambertian Constraints," *IEEE International Conference on Computer Vision*, 1988, pp. 297-302.

[45] Brooks, M.J. "Shape from shading," BKP Horn, Cambridge, MA: MIT press, 1989.

[46] Nayar, S.K., "Determining Shape and Reflectance of Hybrid Surfaces by Photometric Sampling," *IEEE Trans. on Robotics and Automation*, vol. 6, no. 4, 1990, pp. 418-431.

[47] Blake, A., "Shape from Specularities: Computation and Psychophysics," *Phil Trans R. Soc. Lond*on. vol. 331, pp. 237-252, 1991.

[48] Nayar, S.K., "Shape from interreflections," *Int. Journal of Computer Vision*, vol. 6, no. 3, 1991, pp. 173-195.

[49] Koenderink, J.J., "Surface Shape and Curvature Scales," *Image and Vision Computing*, vol. 10, no. 8, 1992, pp. 557-565.

[50] Nayar, S.K., "Reflectance based object recognition," *Int. Journal of Computer Vision*, vol. 17, no. 3, 1996, pp. 219-240.

[51] Lu, J., "Reflectance and Shape from Images Using a Collinear Light Source," *Int. Journal of Computer Vision*, vol. 32, no. 3, 1999, pp. 213-240.

[52] Zheng, Q., "Estimation of Illuminant Direction, Albedo, and Shape from Shading," *Computer Vision and Pattern Recognition*, 1991, pp. 540-545.

[53] Savarese, S., "Local Analysis for 3D Reconstruction of Specular Surfaces," *Computer Vision and Pattern Recognition*, vol. 2, 2001, 738-745.

[54] Ragheb, H., "Diffuse Reflectance Models for Rough Surfaces: A Geometrical Study for Shape-from-Shading," *Proc. The 2nd International Workshop on Texture Analysis and Synthesis*, Copenhagen, Denmark, pp. 113-116, June 2002.

[55] Mercier, B., "A Framework for Automatically Recovering Object Shape, Reflectance and Light Sources from Calibrated Images," *Int. Journal of Computer Vision*, vol. 73, no. 1, 2007, pp. 77-93.

[56]   Wolff, L., "Improved Diffuse Reflection Models for Computer Vision," *Int. Journal of.Computer Vision*, vol. 30, no. 1, 1998, pp. 55-71.

[57]   Yu, T., "Shape and View Independent Reflectance Map from Multiple Views," *Int. Journal of.Computer Vision*, vol. 73, no. 2, 2007, pp. 123-138.

[58]   Yoon, K., "Joint Estimation of Shape and Reflectance using Multiple Images with Known Illumination Conditions," *Int. Journal of.Computer Vision*, vol. 86, no. 2-3, 2010, pp. 192-210.

[59]   Smith, W., "Estimating Facial Reflectance Properties Using Shape-from-Shading," *Int. Journal of.Computer Vision*, vol. 86, no. 2-3, 2010, pp. 152-170.

[60]   Nayar, S.K., "Removal of Specularities Using Color and Polarization," *Computer Vision and Pattern Recognition*, 1993, pp. 583-590.

[61]   Lin, S., "A Representation of Specular Appearance," *IEEE Int. Conf. on Computer Vision*, Kerkyra, Corfu, Grece, pp. 849-854, 1999.

[62]   Lin, S., "Estimation of Diffuse and Specular Appearance," *IEEE Int. Conf. on Computer Vision*, Kerkyra, Corfu, Greece, pp. 855-860, 1999.

[63]   Lin, S., "An Appearance Representation for Multiple Reflection Components," *Computer Vision and Pattern Recognition*, vol. 1, 2000, pp. 105-110.

[64]   Ragheb, H., "Separating Lambertian and Specular Reflectance Components Using Iterated Conditional Modes," *In Proc. British Machine Vision Conf.*, Manchester, UK, 2001, pp. 10-13.

[65]   Nayar, S.K. "Diffuse Structured Light," *2012 IEEE Conf. on Computational Photography (ICCP)*, Cluj-Napoca, Romania, pp. 1–11, 2012.

[66]   Calabi Yau Systems. (2013, Dec 26), *LD3 Studio*, http://www.calabiyausystems .com/ Products-LD3Studio.aspx#!/page_products_ld3studio

[67]   Bentley Systems Website, (2013, Dec 12), *Microstation Productline*. [Online]. http://www.bentley.com/en-US/Products/microstation+product+line/

CHAPTER 3

FOURIER ERROR ANALYSIS OF RAY TRACING ON A GEOSPATIAL

POLYGONAL MODEL[1]

Fourier Error Analysis of Ray Tracing on a Geospatial Polygonal Model

Brandon J. Baker, *Student Member, IEEE*

Abstract— This paper demonstrates that the error associated with ray tracing photorealistic polygonal models of Light Detection and Ranging (LIDAR) scan data is negligible for many applications. In some cases, the standard deviation of error is actually reduced by ray tracing to points on a polygonal model between LIDAR data rather than capturing more data from a scanner. Numerical analyses on the sources of error were performed using Fourier analysis, Taylor expansion, and a statistical model of LIDAR data. Ray tracing was then used to calculate the intersection of each polygon at a point of interest, allowing 3D data to be quantified at any location in between LIDAR points. Actual acquired from a LIDAR scanner and modeled data are then compared to the ray traced values. Results show that many data types have sufficiently low spectral content, allowing accurate representation of 3D data acquired from a LIDAR scanner as a polygonal model.

Index Terms—Light Detection and Ranging (LIDAR), error analysis, sensor signal processing, digital terrain model (dtm)

I. INTRODUCTION

THERE is a need for greater understanding of the error associated with the processing of data acquired by light detection and ranging (LIDAR) scanners [1], even though LIDAR scanners have acquired 3D spatial data for surveys, planning, development, inventory control and other applications for over a decade. An error analysis of modeling LIDAR data from terrestrial scanners is presented in this paper.

When a particular application requires additional accuracy, the solution typically involves scanning at a higher resolution of 3D spatial data. This reliance on data directly acquired from LIDAR scanners has forced many users to gather redundant data at the expense of efficiency. This paper explores the sources of error associated with LIDAR data and the effects of ray tracing polygonal LIDAR data as an alternate to acquiring and utilizing high density scans. The errors are quantified for a paved surface; however the results may be applied to many other types of surfaces.

The results of this analysis demonstrate that polygonal models of terrestrial LIDAR data are accurate methods for representing DTMs. The results further demonstrate that the accuracy of a polygon created from LIDAR data can be higher than scanning at a higher resolution for many applications.

II. PREVIOUS RESEARCH

Many researchers have performed error analyses on various algorithms that process aerial LIDAR scanning data [1]-[8]. In reference [1], the authors analyze various algorithms used to estimate spatial data from LIDAR data to create DEMs and DTMs. These previous works describe observations of error in specific environments but do not provide a complete mathematical basis to address the reasons why the particular results were observed. Additional publications discuss the processing of airborne LIDAR data for DTM extraction [9]-[11]. Reference [9] analyzes LIDAR data DTM extraction via adaptive processing; [10] discusses modeling of LIDAR waveforms in vegetation populated terrains; [11] offers insight into techniques for analyzing bathymetric LIDAR data.

This paper explains the mathematics behind estimation theory as it applies to LIDAR scan data, and offers several illustrative examples of the errors associated with actual and modeled scan data to make an accurate assessment of the strengths and limitations of ray tracing on polygonal models.

III. DATA DESCRIPTION AND ANALYSIS

A. Initial Error Estimates Using Actual LIDAR Data

The LIDAR data chosen for this project are taken from a paved surface. Two separate LIDAR scans taken from the same location were captured a few minutes apart. Data from one scan were thinned and polygonal models were generated to represent a surface. The discrepancy between the acquired LIDAR data and the ray trace calculation were determined. The difference between LIDAR points from one scan to another, captured from the same location, was also computed. The differences were plotted as a function of distance from the scanner, up to 25m, as shown in Fig. 1. The LIDAR to LIDAR difference exceeded that of the ray trace to LIDAR difference for every distance plotted.
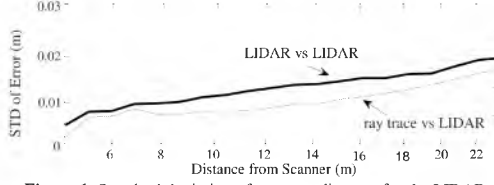
Figure 1. Standard deviation of error vs. distance for the LIDAR vs. LIDAR and ray trace vs. LIDAR examples

The discrepancies between the two plots found in Fig. 1 are the result of low pass filtering. Inherent noise in LIDAR scanners can be reduced on relatively flat surfaces by creating polygons from lower resolution LIDAR points.

IV. ANALYSIS OF THE SOURCES OF ERROR

A. Overview

In general, there are fundamentally three sources for error when acquiring data. The first is discretization; this source was quantified using Fourier analysis. Second, the method applied in utilizing the data (connecting the dots), which was quantified using Taylor's expansion. Third is the inaccuracy inherent in the acquisition process, which was analyzed using statistical methods. Models of anomalous elements, a groove, a bump, and an inclined plane, were created and the corresponding Fourier spectra were analyzed.

B. Fourier Analysis of Error Due to Finite Sampling Rate

Using one dimensional Fourier analysis, a finite number of harmonics (N) can construct a function within an error of ε_N,

$$\varepsilon_N = \sum_{n=N+1} A_n \cos(\omega_n \phi) + B_n \sin(\omega_n \phi) \cdot \qquad (1)$$

ω_n is the spatial frequency, ϕ is the azimuth angle, and A_n and B_n are the amplitudes of the even and odd functions in the series, respectively. Dimensions of the various models are given in Table I. Fig. 2 and Fig. 3 depict a cross section of the groove with its corresponding Fourier spectra, respectively. The standard deviation of various errors due to band-limiting, (1), of modeled data for the anomalous groove were calculated for various sampling rates (Fs) and distances (d), and are given in Table II below.

Figure 2. Model of an anomalous groove in a paved surface
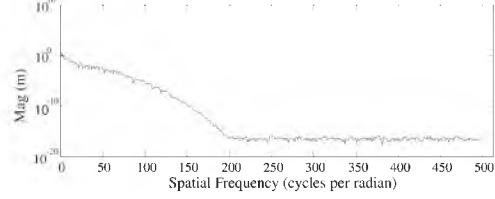
Figure 3. Fourier spectrum of anomalous groove from Figure 2

At 50m the standard deviation of the band-limiting error exceeds that of the maximum height of the anomaly itself. However, at that same sampling rate, the standard deviation of band-limiting error is less than a millimeter when capturing at or below a distance of 10m.

The bump modeled for this project is similar to the rough surface of pavement due to the shape of the pieces of gravel that are compacted as the road is made. The calculated errors of ray tracing polygonal approximations of the bump are given in Table III. These errors suggest that one must scan at an extremely high resolution from two meters away to achieve sub-millimeter accuracy when modeling a small anomaly.

The slightly curved incline in the paved surface is used to represent the slight crowning of a roadway that elevates towards the center of the road. The incline rises approximately 15mm over a span of 1m. The computed errors for the incline are given in Table IV. The errors in Table IV seem extraordinarily high. However, this simply suggests that the reconstruction of an inclined surface should be accomplished by a means other than Fourier. The next section shows that the linear approximation is much better than the band-limited approximation for the modeled incline.

TABLE I.

Anomaly	Width	Height
Groove	428mm	21mm
Bump	8.56mm	11.5mm
Incline	500mm	25mm

TABLE II.

Fs	d	ε_N
1,000 S/rad	2m	6.268 x 10-17 m
1,000 S/rad	5m	2.0163 x 10-6 m
1,000 S/rad	10m	6.2542 x 10-4 m
1,000 S/rad	50m	2.86 x 10-2 m

TABLE III.

Fs	d	ε_N
10,000 S/rad	2m	3.278 x 10-4 m
10,000 S/rad	3m	1.153 x 10-3 m
10,000 S/rad	5m	2.717 x 10-1 m
10,000 S/rad	10m	5.00 x 10-1 m

TABLE IV.

Fs	d	ε_N
1,000 S/rad	2m	6.268 x 10-17 m
1,000 S/rad	5m	2.0163 x 10-6 m
1,000 S/rad	10m	6.2542 x 10-4 m
1,000 S/rad	50m	2.86 x 10-2 m

C. Error Due to Linearization

The preceding error estimation in (1) assumes that the function, $f(\phi)$ is approximated using sine's and cosines. However, for this project, the function $f(\phi)$ is represented by planar surfaces (triangulated 3D polygons), which can be reduced to lines when analyzing LIDAR data as a function of azimuth angle only.

The error of a linear approximation to any function can be quantified by using Taylor's expansion of the Fourier sine and cosine series. Taking the nonlinear terms of a particular frequency of cosine or sine, respectively, yields for each A_n and B_n, respectively, the total error associated with the polygonal (linear) approximation. Thus,

$$\varepsilon_{Lin} = \sum_{n=1}^{N} A_n \sum_{m=1}^{\infty} \frac{(\omega_n \phi)^{2m}}{(2m)!} + \sum_{n=1}^{N} B_n \sum_{p=1}^{\infty} \frac{(\omega_n \phi)^{2p+1}}{(2p+1)!} \qquad (2)$$

the sum of which constitutes the linearization error for odd and even, non-linear functions, respectively.

The total error, then, of the polygonal model versus the true paved surface can be quantified by summing the errors from (1) and (2). Finally, the surface of the paved surface, $f(\phi)$, can be represented as a function of the terms used in the polygonal (linear) approximation and the total error, as

$$f(\phi) = \sum_{n=1}^{N} \left(A_n + B_n \omega_n \phi \right) + \varepsilon_N + \varepsilon_{Lin} \cdot \qquad (3)$$

A few of the results are given in Table V. The standard deviation of the total error for each model shows that the ill-effects of polygonalization can be neglected in many cases. In cases where the total error is less than the error due to band-limiting, one can assume that the linear approximation to the surface is a better approximation than the Fourier reconstruction, and thus the error is reduced when linearized.

The standard deviation of the total error for the anomalous bump as captured from $2m$ away with a sampling frequency of 1,000 S/rad was calculated to be $0.599mm$ (as shown in Table V). The linear approximation and original model for the anomalous bump is shown below in Fig. 4.

One can recognize from Fig. 4 where the largest errors are due to the polygonalization of LIDAR data. However, the standard deviation for these particular settings is still less than a millimeter. The results of this numerical analysis suggest that polygonalization is not the primary source of error in scan data. Rather, limitations due to noise in the scanning hardware contribute far more to the overall error in the data than polygonalization. In fact, polygonalization can actually reduce the error of scan data for certain objects.

TABLE V.

Anomaly	Fs	d	$\varepsilon_N + \varepsilon_{Lin}$
Groove	1,000 S/rad	50m	0.474mm
Bump	1,000 S/rad	2m	0.599mm
Incline	1,000 S/rad	50m	0.008mm
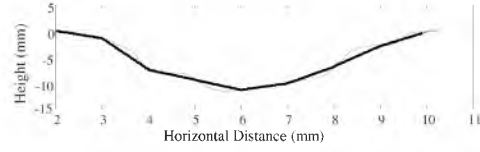
Figure 4. Modeled surface anomaly (bump) and linear approximation

D. Error Due to Scanner Noise

The third source of error is the noise inherent in the scanning hardware. The polygonal model of the inclined plane shown in Fig 5 had a standard deviation of error of $10mm$. The noise in the data can be easily seen in the Fourier spectrum of a sample of data, as shown in Fig. 6.

By comparing the results of the data in Fig. 6 to the model in Fig. 5 of paved surface data, it can be readily seen that there is noise in the higher frequency bands in the actual data. If a perfectly flat surface were scanned, a time of flight scanner would still have errors from $6mm$ to $15mm$, without further processing.

Contrastingly, reducing the sampling rate of the LIDAR data by polygonalization effectively removes the high frequency noise for relatively flat surfaces. Anomalous objects as small as or smaller than the noise region are difficult to detect in a single scan due to the random distribution of frequency components present in the noise. However, utilizing the statistical law of large numbers one could uncover anomalous elements within a series of scans of the same object or scene, even if the size of the object(s) were smaller than the level of noise.

E. The Law of Large Numbers

The Law of Large Numbers mentioned above describes the evolution of statistical behavior as the number of samples in a set of random variables increases. It states that the average of a set of random variables approaches its statistical mean as the number of samples in the set increases.
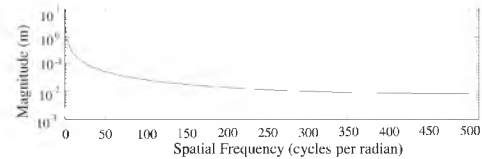
Figure 5. Fourier spectrum of the gradual incline
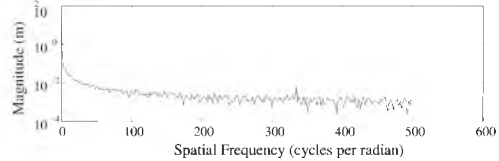
Figure 6. Fourier spectrum of a single horizontal slice of LIDAR data on a paved surface

To illustrate this concept, a set of samples of normally distributed random data, representing range data captured by a scanner with a standard deviation of error of 6mm, was analyzed. The errors of the first sample were not averaged. The errors of the next three sets of samples were then analyzed taking averages of 10, 100, and 1,000 points, respectively. A normalized probabilistic curve for each sample set is shown below as Fig. 7.

One can see the wide distribution of error for the first data set; roughly 67% of the samples have magnitudes of errors less than 6mm. The next set of sample data (upper right of Fig. 15) quantifies the error distribution of samples that have been averaged over 10 points.

The standard deviation of this sample set was calculated to be 1.9mm. Likewise, the third and fourth sets of random data (lower left and lower right of Fig. 7, respectively) correspond to smooth surfaces that are defined by 100 and 1,000 LiDAR points, respectively. The corresponding standard deviations of these data sets were computed to be 0.6mm and 0.19mm, respectively. Resultantly, when scans are processed accordingly, the accuracy can actually be better than the error tolerances published for the scan hardware. Beam divergence also plays a role in the ability to acquire high detail at far distances and could be explored as an additional source of error; however, an analysis of beam divergence is beyond the scope of this paper.

Although it may not practical to scan a scene or surface 1,000 times, the principle holds true that the data converge to the true values as the number of samples increases. This principle can be utilized to recover information that exists below the noise level of the hardware to further optimize a data set.

V. CONCLUSIONS

An error analysis of polygonal models created from actual and modeled terrestrial LIDAR data was performed. Ray traced points were compared to actual LIDAR scan data and modeled data using Fourier spectra, Taylor expansion and statistics. The standard deviation of error for the polygonal model of the anomalous groove was 0.474mm; the error for the bump was 0.599mm; and the error for the incline was 0.008mm.

This analysis showed that for objects with few high frequency features, scanning at a higher density actually increases measurement error. Polygonal models can act as filters to remove high frequency noise, thus lowering the errors inherent in LIDAR data utilization. Polygonal models created from LIDAR scan data can thereby be used to accurately represent real world objects. Furthermore, due to the error inherent in LIDAR scanning hardware, polygonal models can actually yield lower standard deviations of error than LIDAR scanning at a higher resolution.

Figure 7. Probabilistic Curves Illustrating the Error of Scan Data

REFERENCES

[1] Smith, S.L., Holland, D.A., Longley, P.A, "The importance of understanding error in lidar digital elevation models", XXth ISPRS Congress, 2004.

[2] Declercq, F.A.N (1996) Interpolation methods for scattered sample data: Accuracy, spatial patterns, processing time. Cartography and Geographical Information Systems 23(3), 128-144.

[3] Desmet, P.J.J (1997) Effects of interpolation errors on the analysis of dems. Earth Surface Processes and Landforms 22, 128-144.

[4] Maas, H-G and Vosselman, G (1999) Two Algorithms for Extracting Building Models from Raw Laser Altimetry Data. ISPRS Journal of Photogrammetry and Remote Sensing 54 (1999) 153-163.

[5] Morgan, M and Habib, A (2002) Interpolation of LiDAR Data and Automative Building Extraction. ACSM-ASPRS 2002 Annual Conference Proceedings.

[6] Rees, W.G. (2000) The accuracy of Digital Elevation Models interpolated to higher resolutions. International Journal of Remote Sensing, vol. 21, no 1, 7-20.

[7] Sandwell, David T., "Biharmonic Spline Interpolation of GEOS-3 and SEASAT Altimeter Data", Geophysical Research Letters, 2, 139-142,1987.

[8] Smith, S.L, Holland, D.A, and Longley, P.A "Interpreting Interpolation: The Pattern of Interpolation Errors in Digital Surface Models Derived from Laser Scanning Data. Proceedings of GISRUK 2003.

[9] Hyun S. Lee, Nicolas H. Younan, "DTM Extraction of Lidar Returns Via Adaptive Processing", IEEE TGARS, Vol 41, No 9, Sept 2003.

[10] Wenge Ni-Meister, David L. B. Jupp, and Ralph Dubayah, "Modeling Lidar Waveforms in Heterogeneous and Discrete Canopies", IEEE Transactions on Geoscience and Remote Sensing, vol 39, No. 9, Sept 2001.

[11] Wong, H., and Andreas Antoniou, "One-Dimensional Signal Processing Techniques for Airborne Laser Bathymetry", IEEE TGARS, Vol 32, No. 1, Jan 1994.

Brandon J. Baker is a student member of IEEE. He received the BSEE and MSEE degrees from the University of Utah in 1998 and 2003, respectively. He is currently pursuing the Ph.D. degree at the University of Utah. Brandon is President and CEO of Pinpoint 3D Inc., a LiDAR data processing and visualization company in Salt Lake City, Utah. His current research interests include applied mathematics, geospatial modeling, Light Detection and Ranging (LIDAR) data analysis, and numerical inversion theory. He has held positions as faculty in the Department of Mathematics at the University of Utah and Brigham Young University, as a research scientist at LiveWire Test Labs, as an ASIC design engineer at Evans and Sutherland, and a project engineer at InteliSum. He is the inventor or co-inventor of 16 pending patents.

CHAPTER 4

DETERMINING REFLECTANCE PROPERTIES OF

INDUSTRIAL PLANT PRIMITIVES[1]

4.1 Abstract

This paper outlines a method for determining reflectance parameters for modeling

and rendering industrial plant primitives. The reflectance parameters are diffuse and

specular material properties and the industrial plant primitives are pipes from raw LiDAR

brightness data. For diffuse reflectance, the Lambertian model is compared to the Oren-

Nayar model, and methods for estimating both are presented. For specular reflectance,

the Phong model, commonly used in computer graphics, is used. The brightness data

acquired from LiDAR systems are modeled as two different ideal cylinders to recover the

diffuse and specular reflectance parameters and to illustrate the proposed method. A

measured cylinder using brightness data acquired from a LiDAR scanner is also

analyzed, and the diffuse and specular reflectance parameters are estimated. The estimate

for the specular coefficient and exponent of the ideal cylinder are within 3.5% and 3.6%,

respectively and the estimate for the Lambertian reflectance albedo for the ideal cylinder

is within 0.02% of the actual value. The estimate for the diffuse reflectance and

roughness parameters for the second ideal cylinder are within 0.3% and 1.2%, respectively. The estimated reflectance model of the measured cylinder has a mean relative error of 2.88% and a standard deviation of relative error of 4.0%.

4.2   Introduction

As-built models of industrial plants are utilized extensively in asset management, asset virtualization, risk assessment, and emergency evacuation planning and training [7], [14], [42]. "As-builts," as they are commonly called, are databases containing existing condition information about a natural or human architected structure. Ascertaining as-built information for industrial plants usually involves taking measurements, utilizing those measurements to create geometric primitives (such as pipes, flanges, elbows etc.), annotating those primitives with descriptive information, and storing the results in a database for future use. This paper proposes methods for estimating specular and diffuse reflectance properties for pipes, the simplest and most prevalent of all industrial plant primitives.

Specular reflectance is the modeling of light as it reflects off a surface at a single (or very limited number of) angle(s). Specular reflectance describes an object's "shininess." Diffuse reflectance is the reflectance of light that scatters in many angles, is not "shiny," and is largely responsible for illustrating the contrast between brightness and darkness of the colors we see in objects.

Estimating specular and diffuse parameters has been performed for geometric modeling applications, where these two physical aspects of reflectance are determined independent of each other [37]. The purpose of determining the reflectance properties in

that paper was to help determine the shape of the object under inspection. The shapes of primitives in industrial plants can be created in a similar manner using photogrammetric methods [7], a hybrid of photogrammetry and LiDAR [11], or solely from LiDAR range images [9].

Once the geometry has been determined, the photorealistic attributes of geometric primitives are seldom utilized in industry today [42]. In fact, few existing computer aided design (CAD) visualization and utilization tools are even capable of properly rendering the specular and diffuse material properties of 3D CAD models (Toro et al. 2006).

Modern CAD models for industrial plants contain much more than simple geometric primitive information. Such information may include: material type, outer diameter, inner diameter, material density, melting point, specific heat, purchase price, purchase date, or life expectancy. If the specular and diffuse reflectance values of the industrial plant primitives in their current state were known, the material type could be automatically estimated. The material properties such as density, melting point, specific heat, life expectancy, or even the inner diameter could be automatically estimated (when utilized in conjunction with geometric information such as a cylinder's outer radius) once they are identified with a matching material type in a database library.

All the methods found in the literature that determine reflectance properties of an object do so utilizing photogrammetric methods. The object's shape and the light source(s) illuminating it are typically unknown, and the shape and light source have to be estimated along with the reflectance properties. The methods found in the literature that create CAD models of industrial plants focus on acquiring geometry; the visual aspect is of secondary concern. Furthermore, when a visual element is added to the model, raw

photographic imagery is typically draped over the geometry as a texture map; no material reflectance properties are estimated [9], [11], [7].

The methods outlined in this paper automatically extract specular and diffuse material properties from raw LiDAR data of pipes found in industrial plants. The sizes and spatial orientations of the pipes are assumed to be known, and the location and direction of the active light source emanating from the LiDAR scanner illuminating the pipes are also known. The determination of specular and diffuse reflectance properties is the sole objective of this paper, thus differing from related work found in the literature.

In Section 4.3, more details regarding related work found in the literature is presented. Section 4.4 outlines some details of industrial plant modeling of cylindrical objects such as pipes, railings, supports, etc., where the specific mathematical representations of specular and diffuse reflectance models are provided and described. Section 4.4.1 illustrates the difference between the Oren-Nayar and Lambertian diffuse reflectance models.

The numerical inversion process used in this paper is described in Section 4.5. The experimental results are outlined in Section 4.6. Reflective properties from two simulated ideal cylinders and a measured cylinder were determined. The first ideal cylinder was created to illustrate Phong specular and Lambertian diffuse reflectance. The second ideal cylinder was created to illustrate the differences between the Lambertian model and the more general Oren-Nayar model for diffuse reflectance. The final piece in this section outlines experimental results estimating specular and diffuse reflectance values of a measured cylinder using data acquired from a LiDAR scanner of an industrial plant pipe. Section 4.7 contains conclusions and lists potential future work.

4.3   Related Research

Properties of light as they interact with an object and are perceived by human eyes have been researched for centuries [20], [15], [26], [19]. Lambert offered a basic mathematical model that describes this interaction, and the Lambertian model is the most prevalent algorithm for computing diffuse reflectance today [20]. The Lambertian model calculates the brightness of a particular point on an object based on the object's inherent color, the reflected angle of the light source, and its relation to the angle of the viewing direction. The visual properties of light, such as Lambertian reflectance, were applied to computer systems to enhance realism in computer graphics in the 1960s. Cook, Torrance, Sparrow, Phong, and Blinn contributed a great deal of pioneering work in the field [3], [8], [36], [35]. The efficient approximation of specular reflectance is one aspect of early advances in computer graphics that has withstood the test of time.

Oren and Nayar introduced a generalization of Lambert's solution to the diffuse reflectance model by accounting for rough surfaces that scatter light more prevalently than other relatively smooth surfaces [35]. This contribution, although not as computationally efficient as the Lambertian model, provides a much more accurate representation for rough surfaces.

Applications utilizing diffuse and specular reflectance models have yielded advances in the field of determining the geometric properties of an object [12], [18], [13], [10], [4], [6], [28], [2], [32]. [16], [31], [25], [47], [39], [38], [27], [43], [45], [44], [40]. "Shape from shading," as it is more commonly called, has seen dramatic advances over the years. Specular highlights, specifically, can provide detailed and accurate

information regarding the detailed shape of a surface in addition to its reflective properties. Nayar et al. uses reflectance to perform object recognition [31].

The general science of specular and diffuse reflectance has seen significant attention. Brelstaff et al. have utilized Lambertian constraints to detect specular reflection parameters [3]. Nayar et al. have published work relating the surface reflection parameters of a model to its physical and geometrical properties [30]. Soon thereafter, Nayar et al. contributed additional work outlining the identification and removal of specular highlights using color and polarization [29]. Wolff, Nayar, and Oren then published work that applies their enhanced reflectance models for computer vision [43]. Lin and Lee provide several methods for enhancing the visual appearance of objects utilizing specular and diffuse properties [22]-[24]. Ragheb et al. illustrated a method for separating Lambertian and specular reflectance parameters for Machine Vision [37]. More recently, Nayar outlined a method for overcoming challenges in shape from shading techniques using a diffuse filter to alleviate specular highlights and shadowed regions common in digital images [28].

Other efforts have been made to model primitive objects found in industrial plants. Goulette automatically modeled CAD primitives found in industrial pipes using range images [9]. Hong similarly outlined how to obtain 3D models from industrial piping systems using digital photogrammetry in conjunction with laser scan data [11]. Chapman et al. presented an omni-directional imaging system for modeling industrial plants [7].

Previous methods for modeling industrial plant primitives focus on determining the objects' the geometry – size of pipe, orientation in space, its clearance from other

objects, etc. This paper uses LIDAR data similar to [9] and [11], but we determine diffuse and specular reflectance properties instead of primitive geometry. The reflectance properties determined by methods outlined in this paper may enable one to more render realistic models more efficiently and determine the nature and well-being of primitive objects in industrial plants.

4.4   Industrial Plant Cylinder Modeling

One of the most common and most basic primitive forms in industrial plants is the cylinder. Pipes, railings, conduit, heating and cooling ducts, to name a few, are all cylindrical. The typical geometric aspects of a CAD model of a cylinder are shown in Figure 4-1. We use a centerline vector, $\bar{c}$; a radius r; a starting point (not shown); an extrusion or length, l; a surface normal vector, $\vec{k}$; a light source vector, $\bar{s}$; and a light reflection vector, $\bar{R}$. The reflectance properties for our model include: the specular coefficient, S (a scalar), and exponent, n; and the diffuse coefficient (albedo), ρ, and surface roughness coefficient, σ.

Figure 4-2 shows some geometric elements used in the Oren-Nayar model. θ_i is the azimuth incident angle, θ_r is the azimuth reflected angle, ϕ_i is the polar incident angle, ϕ_r is the polar reflected angle, $\vec{k}$ and $\vec{S}$ are the same as in Figure 4-1, and $\vec{i}$ and $\vec{j}$ are orthogonal vectors tangential to the surface of the cylinder. A planar surface is shown in Figure 4-2, depicting a small area where the surface is a plane in the limit.

The specular brightness of a surface (k_{spec}) is defined by the Phong model [36] given by

$$k_{spec} = S(\bar{R} \cdot \bar{V})^n. \tag{4-1}$$

A sample (ideal) cylinder is created and used for Sections 3.5.1 and 3.5.2. Various reflective properties are assigned to the ideal cylinder, to which noise is added, and then the assigned reflective properties are determined by numerical inversion. Next, in Section 3.5.3, LiDAR data of an actual measured cylinder from an industrial plant are used to create a geometric model, from which the reflective properties are determined by numerical inversion.

Since LiDAR scanners typically operate in the infrared or near infrared spectrum, passive light in the visible spectrum (from overhead lights, for example) will not interfere with the near infrared active light source provided by the LiDAR scanner. Due to the nature of LiDAR scanners, the emitting and detecting origins are identical, and likewise, the emitting and detecting paths are coaxial.

The Lambertian diffuse reflectance ratio L_d can be expressed as:

$$L_d = \frac{L_r}{L_i} = \frac{\rho}{\pi}\cos(\theta_i),$$ **(4-2)**

where L_r is the red, green, or blue color value received at the sensor for a color imaging device, or the brightness value received in the LiDAR case (where the intensity of the reflected light is mapped in grayscale); L_i is the intensity of light emanating from the source; L_d is the ratio of reflected light versus emitted light; ρ is the diffuse coefficient (albedo); θ_i is the azimuth incident angle; *and* L_r is the resulting brightness [20]. Typically, a LiDAR scanner will record the ratio L_d/L_i as a unitless reflectance ratio, so we will use that quantity as the diffuse contribution to the "brightness" or the diffuse component of the "data vector." In this paper, we utilize the quantity ρ/π frequently for convenience, even though ρ is the "albedo."

The Oren-Nayar generalized reflectance model [35] can be expressed as:

$$L_d = \tfrac{\rho}{\pi}\cos\theta_i\,(A + (B\max[\,0,\cos(\phi_i-\phi_r)]\sin\alpha\tan\beta\,)) \qquad \text{(4-3)}$$

where

$$A = 1 - 0.5\tfrac{\sigma^2}{\sigma^2+0.33}, \qquad\qquad\qquad \text{(4-4)}$$

$$B = 0.25\left(\tfrac{\sigma^2}{\sigma^2+0.09}\right)\left(\tfrac{4\alpha\beta}{\pi^2}\right)^2, \qquad\qquad \text{(4-5)}$$

$$\alpha = \max[\,\theta_r,\theta_i\,],\ \text{and} \qquad\qquad\qquad \text{(4-6)}$$

$$\beta = \min[\,\theta_r,\theta_i\,]. \qquad\qquad\qquad\qquad \text{(4-7)}$$

where ρ is the diffuse coefficient (albedo), and σ is the surface roughness coefficient.

The Oren-Nayar reflectance model (4-3) simplifies to the Lambertian model (4-2) when $\sigma = 0$. The physical interpretation of σ is the standard deviation of the gradient of the surface elevation or slopes of the rough surface and thereby its upper limit is unbounded. An additional simplification can be made since the emitting and detecting axes and origins are identical for LiDAR scanners. This suggests that $\theta_i = \theta_r$ and $\phi_i = \phi_r$; thus, (4-3) reduces to

$$L_d = \tfrac{\rho}{\pi}\cos\theta_i\left(A + (B\sin\alpha\tan\beta)\right). \qquad\qquad \text{(4-8)}$$

4.4.1   Colorless Specular and Diffuse Determination by Numerical Inversion

Brightness values for an ideal cylinder with Lambertian diffuse reflectance and an ideal cylinder with Oren-Nayar diffuse reflectance (both without specular reflectance) are shown in Figure 4-3 to emphasize the difference between the two models. The brightness values arranged as pixels in an image are shown in Figure 4-3. These brightness values are the data vector values, d, that will be used in the inversion process in the next section. The parameters of ideal cylinders for the Oren-Nayar diffuse model (left) are: $\rho/\pi = 0.5$, $\sigma = 0.25$, $S = n = 0$; and Lambertian model (right); $\rho/\pi = 0.5$, $\sigma = 0.0$, $S = n = 0$.

Figure 4-4 shows brightness values along a cross section of the pipe, with the mean of intensity values at a given horizontal distrance from the pipe center plotted for the Oren-Nayar and the Lambertian models. The intensity rounds off gradually as the angle of incidence strays from the center for the Lambertian reflectance; whereas, the Oren-Nayar model (represented as a dash-dotted line) tapers off slowly around the center of the pipe, and then drops abruptly at the edges.

Figure 4-4 illustrates the reflectance values shown in Figure 4-3 that exist at different radial distances from the center. As shown in Figure 4-3, Figure 4-4 shows the gradual rounds off effect inherent in the Lambertian reflectance; whereas, the Oren-Nayar model demonstrates the slow tapering off around the center of the pipe, and then abruptly drops at the edges. Whereas the Oren-Nayar is more computationally intense, it also provides a more general characterization of an object's diffuse reflectance properties, so it should provide added information that the Lambertian does not.

4.5   Numerical Inversion Process

Numerical inversion is an iterative process by which a set of unknown model parameters, *m*, can be estimated by using an initial guess of the model parameters and a known forward operator, $A(m)$. The forward operator provides an approximation, $\hat{d}$, to the data vector, d, and the difference between the d and $\hat{d}$ (in some sense) provides an update to the model parameters for the next iteration. The forward operator for the inverse problems found in this paper is

$$\hat{d} = A(m) = k_{spec}(S,n) + L_d(\rho/\pi,\sigma),$$
(4-9)

where k_{spec} and L_d are determined by (4-1) and (4-8), respectively, and the model parameter vector, m, is $\{S, n, \rho\ \sigma\}$.

The forward operator for this problem is a nonlinear process, so a nonlinear inversion technique must be employed. Conjugate gradient, steepest descent, and Newton's method are a few possible inversion techniques that may be used to solve this problem. For this paper, Newton's method with line search was selected as the numerical inversion algorithm based on its reputation for rapid convergence.

Ideal cylinder #1 was modeled using Phong specular (4-1) and Lambertian diffuse reflectance (4-8). The model parameter vector $\{S, n, \rho/\pi\}$ for ideal cylinder #1 has specular content ($S = 0.154$, and $n = 26.8$), and a Lambertian reflectance coefficient of $\rho/\pi = 0.498$. We created the ideal model using brightness data calculated by (4-9) with the parameter values given above, then added 1.45% standard deviation of Gaussian noise. For this cylinder, (4-9) becomes:

$$A_L(m) = S(F \cdot V)^n + \frac{\rho}{\pi}\cos\theta_i \qquad (4\text{-}10)$$

where $\sigma = 0$.

Ideal cylinder #2 was modeled using only Oren-Nayar diffuse reflectance (4-8) without a specular component ($k_{spec}=0$) to illustrate the differences between the Lambertian model and the Oren-Nayar model. For the numerical inversion of this cylinder (4-9) becomes:

$$A_{ON}(m) = \frac{\rho}{\pi}\cos\theta_i\left(A + \left(B\sin\alpha\tan\beta\right)\right). \qquad (4\text{-}11)$$

where m = $[\rho,\ \sigma]$; A and B are computed by (4-4) and (4-5), and α and β are determined by (4-6) and (4-7).

Finally, the measured cylinder from LiDAR intensity data was modeled using specular and Oren-Nayar model parameters. Newton's method for inverse problems iteratively updates m according to

$$m_i = -inv(F'F)F'(\hat{d}_{i-1} - d),$$ (4-12)

where F is the Frechet derivative of the forward operator, A; and d is the brightness data vector. More information on the Frechet derivative, uniqueness, and Newton's method can be found in [34], [46], [41].

The exit criterion for the inversion process is met when the change in the misfit between iterations is less than 0.0145 divided by the number of elements in the data vector; this corresponds to an average error of 1.45% per datum. LiDAR scanner manufacturers do not publish error metrics of brightness data, so we simply estimate this to be 1.45%.

4.6 Experimental Results

4.6.1 Ideal Lambertian and Specular Model

Figure 4-5 shows the data vector, d, from ideal cylinder #1 and the estimate of the data vector, $\hat{d}$, from the inverted model.

The inversion process, in the presence of noise, was able to estimate the two quantities for specular reflectance (the specular coefficient S and the exponent n) within 3.5% and 3.6% of their actual values, respectively, and the albedo to within 0.02%, as shown in Table 4-1. ($\sigma = 0$ in (4-2), so the final column on the table was not estimated.)

These results correspond reasonably well to the 1.45% standard deviation of noise added to the data vector. The effect of the specular component only affects a relatively

small portion of the surface area of the cylinder (where the bright highlights appear on Figure 4-5), and therefore, a larger specular reflectance error is understandable. Contrarily, the diffuse coefficient affects the entire visible surface of the cylinder; therefore, the error is minimized in the presence of zero mean noise.

4.6.2   Ideal Lambertian and Specular Model

The second ideal model (ideal cylinder #2) uses the Oren-Nayar cylindrical model (4-8) and provides a more generalized estimation of diffuse reflectance phenomena than the Lambertian model by accounting for rough surfaces that exhibit a broader dispersion of light due to surface roughness. Figure 4-6 shows the noisy model (left) compared to the inverted estimate (right).

The ideal noisy cylinder and the inverted approximation have a similar appearance. The diffuse albedo was estimated within 0.3% of the actual value and the roughness was within 1.2% as shown in Table 4-2.

The numerical inversion process described in this paper for estimating reflectance parameters for cylinders (industrial pipes) has proven to effectively determine reflectance parameters in the presence of noise for ideal cylinders. In this section, we considered ideal cylinder models with noise added to the data. In the next section, we perform a similar operation using measured data on a metal pipe found in an industrial plant.

4.6.3   Measured Cylinder

In order to evaluate the Oren-Nayar and Lambertian models in an actual industrial application, LiDAR measurements of a metal pipe vertically aligned, had a radius of 0.20

m, and was covered in light blue paint that exhibited a fair amount of specular reflectance. The LiDAR scanner used was a Leica C10 [21]. The diffuse roughness (σ) of the measured pipe was assumed to be non-zero, so the more general Oren-Nayar diffuse model (11) was used for the inversion process. The albedo (ρ) was 0.498; the measured roughness (σ) was 0.237. The measured specular coefficient (S) was 0.154, and the measured specular exponent (n) was 26.8.

A cross-sectional scatter-plot with all of the brightness values examined for the measured pipe is shown in Figure 4-7. The statistical mean d_m of the data vector, d, and the statistical mean $\hat{d}_m$ of the inverted estimate of the data vector, $\hat{d}$, along the same cross section are shown in Figure 4-8. A detailed plot of d_m and $\hat{d}_m$ in the center section of the measured pipe is shown in Figure 4-9. The error $(|d_m - \hat{d}_m|)$ for the entire cross section of the pipe is shown in Figure 4-10, and the relative error for the entire cross section of the pipe ($|d_m - \hat{d}_m| / \hat{d}_m$) is shown in Figure 4-11.

The inverted values closely resemble the brightness data vector near the center of the pipe where the specular reflection and diffuse reflectance values are maximized. The estimate deviates significantly near the edge of the pipe where the brightness drops below 20%-25% reflectance. This is most likely caused by the nonlinear dynamics of the receiver circuitry. LiDAR scanners possess input signal amplifiers to compensate for the limited dynamic range in the analog to digital conversion process. When the input signal drops below a specified threshold, the analog amplifier boosts the input signal so a reading can be made. The estimate of the roughness coefficient was most adversely affected by this added circuitry. The inversion process attempts to estimate the

brightness of the pipe at the edges, but this nonlinear phenomenon is not accounted for in the estimator model (4-9).

The inverted value for the specular highlight closely matches the brightness data vector. The equation for the specular reflectance (4-1) is used extensively in computer graphics and is not derived from any physics equation, but Figure 4-8 and Figure 4-9 show that it is a close approximation to the actual physical phenomenon exhibited by light reflecting off of specular reflective surfaces. The detail plot of brightness data shown in Figure 4-9 illustrates the effectiveness of the inversion process for specular reflectance in the center of the pipe where the specular reflectance is most pronounced.

The mean relative error (mean of brightness values in Figure 4-12) is 2.88% and the standard deviation of the relative error is 4.0%. The values for each of the inverted model parameters are shown in Table 4-3 .

A photograph of the measured cylinder, its measured LiDAR reflectance values, and the approximated reflectance values obtained by numerical inversion are shown in Figure 4-12, arranged as pixels in an image array.

The photograph demonstrates visual anomalies inherently found in circumstances involving passive light sources. Although there are many light sources present, the dominant light source is above and to the right of the pipe, and there are shadows (and highlights) of other pipes and metal grates visible. A specular highlight appears on the right-hand side of the pipe, just above the middle, as labeled on Figure 4-12. Most of the other variations in brightness are due to highlights and shadows demonstrated by diffuse reflectance.

The center image is LiDAR brightness of the measured pipe. There are obvious anomalies in the actual brightness data due to noise in the receiver circuitry of the LiDAR scanner. One may observe that there are obvious dark regions of similarities between the visible light image (left) and the LiDAR brightness (center). Both sensors failed to return adequate brightness in those regions due to a foreign substance on the pipe in those regions. Also, there is a weld near the bottom of the pipe that is visible in both measured images that is not present in the estimated image (right).

4.7   Conclusions

A method for determining the specular and diffuse reflectance properties for two ideal and one measured pipe from an industrial plant was presented. LiDAR data intensity values provided the brightness data for the measured cylinder. The reflectance properties determined include the specular coefficient and specular exponent commonly used in computer graphics, as well as the diffuse albedo parameter and the Oren-Nayar roughness parameter.

Newton's method from numerical inversion was used to compute the estimate for the model parameters. The inversion process for the ideal cylinders recovered the model parameters within 3.6% of the actual values, providing a suitable method for recovering reflectance parameters.

Inversion of the model parameters for the measured cylinder provided an accurate estimate to the actual data to within 3.5% for all brightness values over 0.3. The relative errors associated with brightness estimation for data at the extreme edges of the pipe,

where the incident angle is close to orthogonal to the surfaced normal, were as high as

44.7% due to nonlinear amplifiers in the detection hardware.

4.8   Acknowledgements

We would like to thank McNeil Engineering for providing the industrial plant data.

4.9   References

[1]   Blake, A., "Geometry from Specularities," *IEEE Int. Conf on Computer Vision, Tampa, FL,* pp. 394-403, 1988.

[2]   Blake, A., "Shape from Specularities: Computation and Psychophysics," *Phil Trans R. Soc. Lond*on. vol. 331, pp. 237-252, 1991.

[3]   Blinn, J. "Models of light reflection for computer synthesized pictures," *Computer Graphics, SIGGRAPH '77 Proceedings,* 187, San Jose, CA, 1977.

[4]   Brelstaff, G., "Detecting Specular Reflection Using Lambertian Constraints," *IEEE International Conference on Computer Vision,* 1988, pp. 297-302.

[5]   Brooks, M.J., "Shape and Source from Shading," *International Joint Conferences on Artificial Intelligence,* Philadelphia, PA, pp. 932-936, 1986.

[6]   Brooks, M.J. "Shape from shading," BKP Horn, Cambridge, MA: MIT press, 1989.

[7]   Chapman, D., "An omnidirectional imaging system for the reverse engineering of industrial facilities," *The International Archives of the Photogrammetry, Remote Sensing and Spatial Information Sciences,* vol. 34, no. XXX, 8 pages, 2004.

[8]   Cook, R., "A reflectance model for computer graphics," *ACM Transactions on Graphics,* vol. 1, no. 1, Jan 1982, pp. 7-24.

[9]   Goulette. F. "Automatic CAD modeling of industrial pipes from range images," *Proc., Int. Conf on Recent Advances in 3- D Digital Imaging and Modeling,* Ottawa, Ontario, Canada, May 1997, pp. 229-233.

[10]   Healey, G.H., "Local Shape from Specularity," *IEEE International Conference on Computer Vision,* 1987, pp. 151-160.

[11] Hong, J. "3D modelling of industrial piping systems using digital photogrammetry and laser scanning," M.S. Thesis, Dept. Elec. Eng., Ryerson Univ., Ottawa, Ontario, Canada, 2003.

[12] Horn, B.K.P., "Determining Shape and Reflectance Using Multiple Images," *Massachussetts Institute of Technology*, 1978, pp. 113-115.

[13] Horn, B.K.P., "The Variational Approach to Shape from Shading," *Computer Vision, Graphics, and Image Processing*, vol. 33, no. 2, 1986, pp. 174-208.

[14] Jorge, C., et al. (2010, Aug 17) *Nuclear Plants and Emergency Virtual Simulations Based on a Low-Cost Engine Reuse. Nuclear Power*, [Online]. Available: http://www.intechopen.com/books/ nuclear-power/nuclear-plants-and-emergency-virtual-simulations-based-on-a-low-cost-engine-reuse

[15] Kerker, M., "The Scattering of Light," New York, Academic, 1909.

[16] Koenderink, J.J., "Surface Shape and Curvature Scales," *Image and Vision Computing*, vol. 10, no. 8, 1992, pp. 557-565.

[17] Koenderink, J.J., "Surface Perception in Pictures," *Perception and Psychophysics*, vol. 52, no. 5, 1992, pp. 487-496.

[18] Koenderink, J.J., The Internal Representation of Solid Shape with Respect to Vision. Biological Cybernetics, vol. 32, 1979, pp. 211-216.

[19] Kubelka, P., „Ein Beitrag zur Optik der Farbanstriche," Zeits. f. Techn. Physik, 12, 593–601, 1931. (see The Kubelka-Munk Theory of Reflectance)

[20] Lambert, J., "Photometria sive de mensure de gratibus luminis, colorum umbrae, " Leipzig, Germany, W. Engelmann, 1760.

[21] Leica Corp., (2013, May 8). *Leica Scanstation C10. Data Sheet*, [Online]. Available: http://hds.leica-geosystems.com/downloads123/hds/hds/ScanStation % 20C10/brochures-datasheet/Leica_ScanStation_C10_DS_en.pdf

[22] Lin, S., "A Representation of Specular Appearance," *IEEE Int. Conf. on Computer Vision*, Kerkyra, Corfu, Grece, pp. 849-854, 1999.

[23] Lin, S., "Estimation of Diffuse and Specular Appearance," *IEEE Int. Conf. on Computer Vision*, Kerkyra, Corfu, Greece, pp. 855-860, 1999.

[24] Lin, S., "An Appearance Representation for Multiple Reflection Components," *Computer Vision and Pattern Recognition*, vol. 1, 2000, pp. 105-110.

[25] Lu, J., "Reflectance and Shape from Images Using a Collinear Light Source," *Int. Journal of Computer Vision*, vol. 32, no. 3, 1999, pp. 213-240.

[26] Mandelstam, L.I., "Light Scattering by Inhomogeneous Media," Zh. Russ. Fiz-Khim. Ova. Ch 58, pp 381, 1926.

[27] Mercier, B., "A Framework for Automatically Recovering Object Shape, Reflectance and Light Sources from Calibrated Images," *Int. Journal of Computer Vision*, vol. 73, no. 1, 2007, pp. 77-93.

[28] Nayar, S.K. "Diffuse Structured Light," *2012 IEEE Conf on Computational Photography (ICCP)*, Cluj-Napoca, Romania, pp. 1–11, 2012.

[29] Nayar, S.K., "Removal of Specularities Using Color and Polarization," *Computer Vision and Pattern Recognition*, 1993, pp. 583-590.

[30] Nayar, S.K., "*Surface Reflection: Physical and Geometrical Perspectives,*" *Pattern Analysis and Machine Intelligence, IEEE Trans., vol.* 13, no. 7, 1991, pp. 611-634.

[31] Nayar, S.K., "Reflectance based object recognition," *Int. Journal of Computer Vision*, vol. 17, no. 3, 1996, pp. 219-240.

[32] Nayar, S.K., "Shape from interreflections," *Int. Journal of Computer Vision*, vol. 6, no. 3, 1991, pp. 173-195.

[33] Nayar, S.K., "Determining Shape and Reflectance of Hybrid Surfaces by Photometric Sampling," *IEEE Trans. on Robotics and Automation*, vol. 6, no. 4, 1990, pp. 418-431.

[34] Oliensis, J., "Uniqueness in shape from shading," *Int. Journal of Computer Vision*, vol. 6, no. 2, 1991, pp. 75-104.

[35] Oren, M., „Generalization of the Lambertian model and implications for machine vision," *International Journal of Computer Vision*, vol. 14, no. 3, 1995, pp. 227-251.

[36] Phong, B., "Illumination for Computer Generated Pictures," *Communications of the ACM*, vol. 18, no. 6, pp. 311-317, 1975.

[37] Ragheb, H., "Separating Lambertian and Specular Reflectance Components Using Iterated Conditional Modes," *In Proc. British Machine Vision Conf*, Manchester, UK, 2001, pp. 10-13.

[38] Ragheb, H., "Diffuse Reflectance Models for Rough Surfaces: A Geometrical Study for Shape-from-Shading," *Proc. The 2nd International Workshop on Texture Analysis and Synthesis*, Copenhagen, Denmark, pp. 113-116, June 2002.

[39] Savarese, S., "Local Analysis for 3D Reconstruction of Specular Surfaces," *Computer Vision and Pattern Recognition*, vol. 2, 2001, 738-745.

[40]   Smith, W., "Estimating Facial Reflectance Properties Using Shape-from-Shading," *Int. Journal of Computer Vision*, vol. 86, no. 2-3, 2010, pp. 152-170.

[41]   Tarantola, A. *Inverse Problem Theory and Methods for Model Parameter Estimation*. Philadelphia, PA: SIAM, 2005.

[42]   Toro, C., "Improving Virtual reality Applications in CAD through Semantics," *The International Journal of Virtual Reality*, vol. 5, no. 4, 2006, pp. 39-46.

[43]   Wolff, L., "Improved Diffuse Reflection Models for Computer Vision," *Int. Journal of Computer Vision*, vol. 30, no. 1, 1998, pp. 55-71.

[44]   Yoon, K., "Joint Estimation of Shape and Reflectance using Multiple Images with Known Illumination Conditions," *Int. Journal of Computer Vision*, vol. 86, no. 2-3, 2010, pp. 192-210.

[45]   Yu, T., "Shape and View Independent Reflectance Map from Multiple Views," *Int. Journal of Computer Vision*, vol. 73, no. 2, 2007, pp. 123-138.

[46]   Zhdanov, M., *Geophysical Inverse Theory and Regularization Problems*. New York, NY: Elsevier Science, 2002.

[47]   Zheng, Q., "Estimation of Illuminant Direction, Albedo, and Shape from Shading," *Computer Vision and Pattern Recognition*, 1991, pp. 540-545.
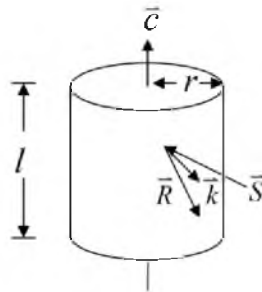
Figure 4-1: Geometric representation of cylinder model
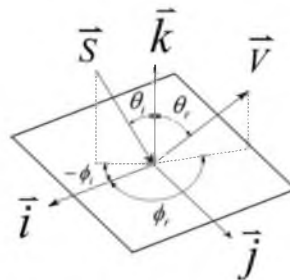
Figure 4-2: Geometric representation for Oren Nayar model
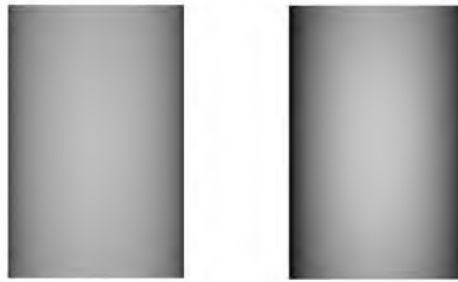
Figure 4-3: Brightness values, d, of ideal cylinders: Oren-Nayar diffuse model (left); and Lambertian model (right);
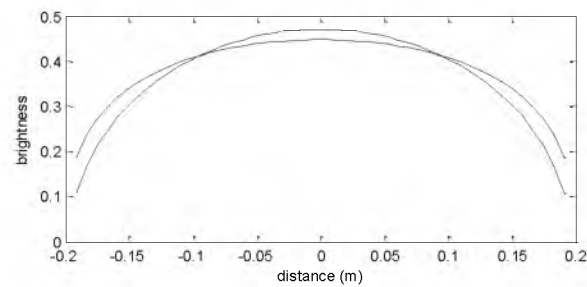
Figure 4-4: Statistical mean for Lambertian reflectance (-•-•) and Oren-Nayar (-) along a cross section of the pipe
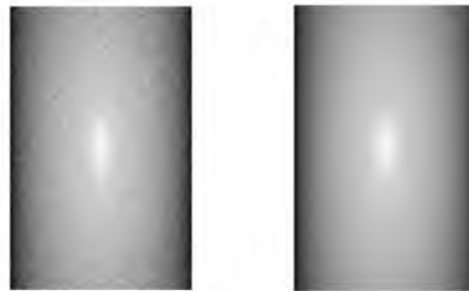
Figure 4-5: Ideal cylinder #1: data vector , d, of Lambertian diffuse and Phong specular reflectance with noise (left), and inverted estimate, (right)
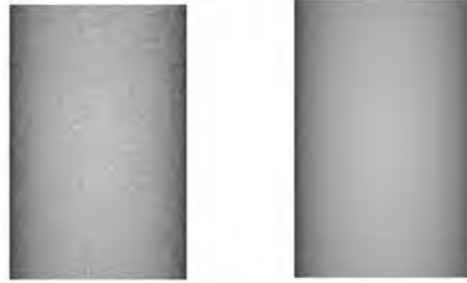
Figure 4-6: Ideal cylinder #2: data vector, d, of Oren Nayar diffuse reflectance with noise (left), and inverted estimate, (right)
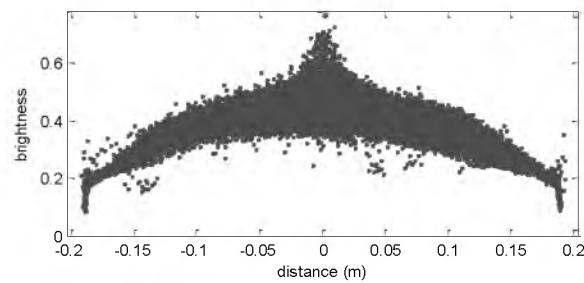
Figure 4-7: Cross section of brightness data vector, d, of measured cylinder
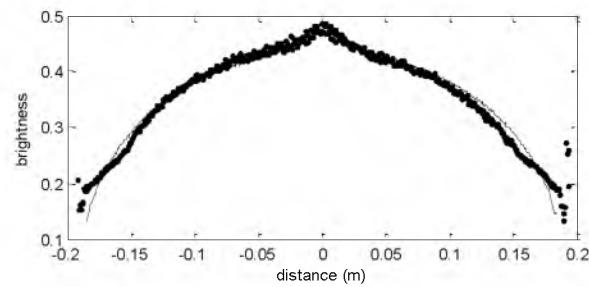
Figure 4-8: Cross section of statistical mean of data vector, dm (dots) and numerical inversion estimate m (line)
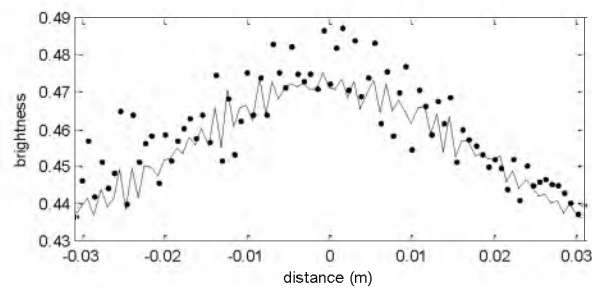
Figure 4-9: Detail of statistical mean of data vector dm (dots) and numerical inversion estimate, m (line), around pipe center
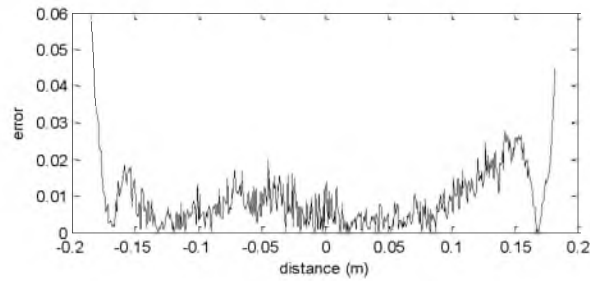
Figure 4-10: Cross section of error of statistical mean $|\, \mathbf{d}_m - \hat{d}_m\,|$
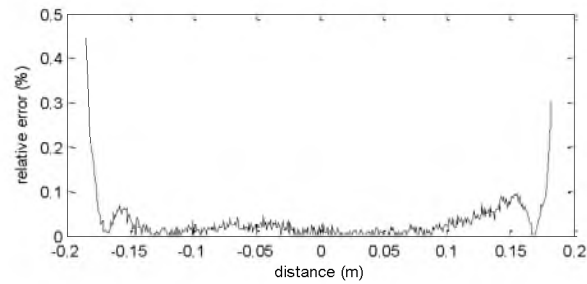
Figure 4-11: Cross section of relative error $|\, \mathbf{d}_m - \hat{d}_m\,| / \hat{d}_m$
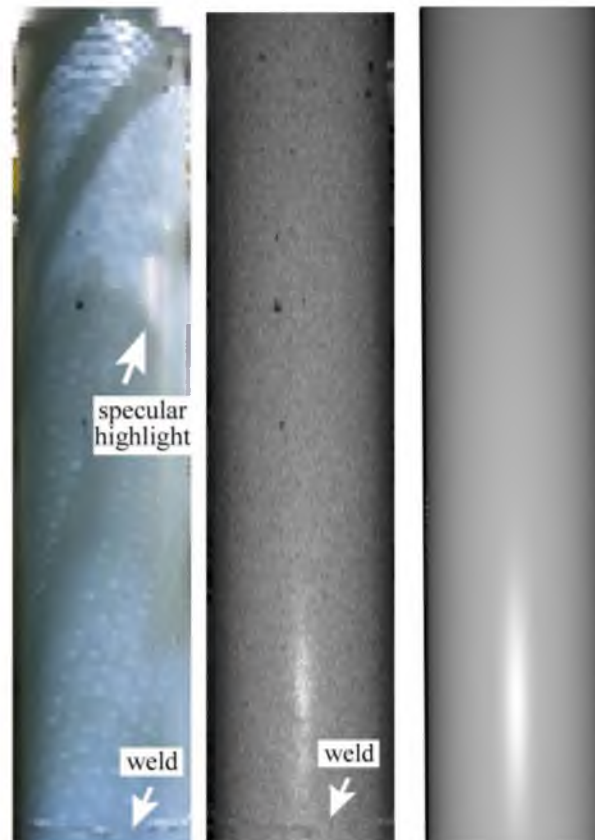
Figure 4-12: Photograph of measured pipe (left); LiDAR brightness data vector, d, (center); and inverted brightness estimate (right)

Table 4-1 Inverted Model Vector, *m*, for Ideal Cylinder #1

	S	n	ρ/π	σ
Ideal	0.150	27.0	0.500	-
Estimate	0.145	25.9	0.499	-
|rel error|	3.5%	3.6%	0.02%	-

Table 4-2 Inverted Model Vector, *m*, for Ideal Cylinder #2

	S	N	ρ/π	σ
Ideal	-	-	0.500	0.250
Estimate	-	-	0.498	0.243
|rel error|	-	-	0.3%	1.2%

Table 4-3 Inverted Model Vector, *m*, for Measured Cylinder

	S	n	ρ/π	σ
Inverted	0.154	26.835	.4980	0.237

CHAPTER 5

DETERMINING SPECULAR, DIFFUSE, AND AMBIENT COLOR

MATERIAL PROPERTIES OF INDUSTRIAL

PLANT PRIMITIVES[1]

5.1 Abstract

This paper describes a method for determining specular, diffuse, and color material properties of industrial plant primitives and applies the method to seven pipes from an industrial plant. The properties are determined in two steps. First, colorless specular and diffuse properties were estimated by numerically inverting LiDAR brightness data. Then, color ambient and diffuse properties are estimated using digital photographs of the pipes using k-means clustering. The colorless properties yielded estimated brightness values that are within an RMS average of 3.4% of the measured data. The maximum RMS residual for the colorless properties was 7.0% and the minimum was 1.6%. The maximum residual occurred on a small (radius = 0.01m) pipe 1.5m away from the scanner, while the minimum occurred on a small (radius = 0.02m) pipe 0.6 meters away from the scanner. The estimated color properties effected an average RMS residual of 13.2% with a maximum of 20.3% and a minimum of 9.1%.

5.2 Introduction

This paper applies the specular and diffuse material property estimation technique described in [1] to several pipes in an industrial plant and introduces a method for determining color material properties from industrial plant primitives. 3D model material properties are difficult to attain yet can be used extensively for visualization in computer graphics systems. These visualization systems are used for Computer Aided Design (CAD) and inspection [2], [26], virtual reality training [3]-[6], and marketing or other walk-throughs [7]-[9]. Automated or semi-automated CAD model generation from industrial plants is a growing area of research and development. Methods used include photogrammetry [10], [11], Light Detection and Ranging (LiDAR) laser scanning [12]-[16], or both [17], [3]. Other applications of 3D model material properties may include automated object recognition, construction progress tracking [18], or object condition assessment [19].

Most CAD models include pipe geometry, visual material properties, and in some cases, information about the model. Although most CAD systems render very simple visual information associated with the model, some systems can render photorealistic textures [22], [23]. Photorealistic models are visually appealing, yet they require large amounts of hard drive and RAM storage space, and are computationally intensive to visualize. Even level of detail (LOD) engines cannot operate efficiently without storing, paging, and purging massive amounts of detailed visual information in real-time. The methods outlined in this paper offer an efficient alternative to point clouds or texture mapping to achieve near photorealistic rendering and minimal storage for 3D models of industrial plant primitives.

The material properties determined in this paper include, specular, diffuse, and color (red, green, and blue). Specular properties consist of a coefficient (S) and an exponent (n). The diffuse properties comprise an albedo (ρ) and a roughness (σ). The ambient color properties determined in this paper are the coefficients α_r, α_g, α_b, for the primary colors of light: red, green, and blue, respectively. The diffuse color properties comprise the colored albedos ρ_r, ρ_g, ρ_b, for red, green, and blue, respectively. The methods outlined in Section 5.3 of this paper are divided into two parts. Section 5.3.1 describes several case studies of the specular and diffuse estimation method proposed in [1] applied to measurement data from seven different pipes found in an industrial plant. LiDAR scan intensity (brightness) data are used to estimate the specular and diffuse material properties. Section 5.3.2 offers a k-means color determination method applied to the same seven pipes. Digital photographic data of the pipes are used to estimate the ambient and diffuse colors. Section 5.4, which is also divided into two parts, offers the results and corresponding discussion of the estimations. Section 5.4.1 presents and describes the results for the colorless specular and diffuse estimation, and Section 5.4.2 presents and describes the results of the ambient and diffuse color estimations. Concluding remarks are provided in Section 5.5.

5.3   Methods

5.3.1   Colorless Specular and Diffuse Determination by Numerical Inversion

As described in [1], determining a pipe's specular (S, n) and diffuse (ρ, σ) material properties by numerical inversion requires a geometric model of the pipe as well as a mathematical model of the laser scanning system. The geometric model for each

pipe was created by isolating measured 3D points from a laser scan of the pipe, and then estimating the pipe's centerline and radius using the Levenberg-Marquardt algorithm for nonlinear optimization [24]. The measured intensity (LiDAR brightness) value for each 3D point was then used to estimate the specular and diffuse material properties of the pipe by numerical inversion.

The specular component of the material properties is modeled by:

$$k_{spec} = S(\vec{R} \cdot \vec{V})^n$$

(5-1)

where S is the specular strength (coefficient), n is the specular exponent, $\vec{R}$ is the reflected vector (the source light reflected off the surface), and $\vec{V}$ is the viewing vector (of the laser scanner's sensor) [21].

The diffuse component is modeled by:

$$L_d = \frac{\rho}{\pi} \cos\theta_i \left(A + \left(B \sin\alpha \tan\beta\right)\right),$$

where

$$A = 1 - 0.5 \frac{\sigma^2}{\sigma^2 + 0.33},$$

$$B = 0.25 \left(\frac{\sigma^2}{\sigma^2 + 0.09}\right)\left(\frac{4\alpha\beta}{\pi^2}\right)^2,$$

$$\alpha = \max[\theta_r, \theta_i],$$

$$\beta = \min[\theta_r, \theta_i].$$

(5-2)

Each salient geometric quantity is illustrated in Figure 5-1, where θ_i is the azimuth incident angle, θ_r is the azimuth reflected angle, ϕ_i is the polar incident angle, ϕ_r is the polar reflected angle, $\vec{k}$ and $\vec{S}$ are the same as in Figure 5-1, and $\vec{i}$ and $\vec{j}$ are orthogonal vectors tangential to the surface of the cylinder.

The steepest descent method was used as the numerical inversion technique. First, the residual r_n (at iteration n) is calculated:

$$r_n = A(m_n) - d,$$ (5-3)

where $A(m_n)$ is the forward operator, d is the measured data vector, and m_n is the model vector. The ascent vector is then calculated:

$$l_n = l(m_n) = F^*_{m_n} r_n, \quad g_n = -F_{m_n} l_n,$$ (5-4)

where $F^*_{m_n}$ is the conjugate transpose of the Frechet derivative of $A(m)$ at iteration n. The step length is then estimated:

$$k_n = \frac{\|l_n\|^2}{\|g_n\|^2}.$$ (5-5)

And finally, the model parameters are updated:

$$m_{n+1} = m_n - W\,k_n l_n$$ (5-6)

where W is a diagonal weighting matrix with non-zero values determined by experiment to be [2, 1exp5, 1, 1] for S, n, ρ, σ, respectively, and the forward operator that yields the estimated data vector is given by:

$$\hat{d} = A(m) = k_{spec}(S, n) + L_d(\rho, \sigma).$$ (5-7)

The model parameters were initialized according to: $S_o = \max(d) - \text{median}(d)$; $n_o = 20$; $\rho_o = \text{median}(d)$; $\sigma_o = 0.1$. The steepest descent method iteratively updates the model parameters until the relative change in the misfit (the norm of the residual) is less than or equal to 1%. Nonlinearities at the edges of the pipe corrupt the results of the calculation [1], so any data that laterally exceed 70% of the pipe's radius are discarded, as shown in Figure 5-2.

5.3.2 Color Determination by K-Means Clustering

The nature of the pipe illumination for LiDAR scan data and photographic differ significantly. LiDAR scanners commonly use a wavelength in the near infrared spectrum which allows the scanner to operate as an active light source – isolated from other electromagnetic interference that may be present in other spectra. Furthermore, the light source and detection mechanism for LiDAR scanners are co-axial, thus simplifying the mathematical representation used to model the scanner. Photographic systems for visible light, however, are extremely complicated.

First, the light may be emanating from a point (a small light), a sphere (a light bulb), a cylinder (a single fluorescent bulb), a rectangular plane (a covered fluorescent fixture), or in parallel waves (the sun), for example. These light sources may operate alone or in any combination and from virtually any location. Furthermore, obstructions occlude direct light casting shadows upon objects. In order to accurately estimate the ambient and diffuse color properties of pipes by numerical inversion, all of these items must be known a-priori – to at least some degree. This is an unreasonable assumption; therefore, an alternative method is proposed.

K-means clustering [25] provides an algorithm for segmenting data into clusters. The photographic measurement data for this paper contain, in general, ambient, diffuse, and specular reflections of the pipes under consideration. The specular highlights, although visible in some images, constitute a statistically small number of data when compared to the amount of ambient and diffuse data. Therefore, the k-means clustering algorithm is directed to segment into two clusters – for ambient and diffuse. An illustration of this process is given in Figure 5-3.

The measured data are divided into two clusters for ambient and diffuse and sorted into 100 histogram bins. The α and ρ estimate for each color are then chosen from the highest non-negligible bin among each cluster. To avoid noise interfering with the results, a non-negligible bin is any bin that is at least 20% of the maximum bin in that cluster.

In cases where the pipe is extremely dark, two clusters are found, but one cluster contains diffuse data and the other (an extremely small number of points, by comparison) contains specular data, so the brighter cluster is ignored, the diffuse parameters are estimated based on the darker cluster, and the ambient terms are set to zero. One cluster is determined to be too small if it contains less than ten percent of the number of points when compared to the other cluster. Since this only occurs with dark pipes, this has been determined to be a reasonable method for distinguishing dark pipes from light.

5.4   Results and Discussion

5.4.1   Colorless Specular and Diffuse Properties

Colorless specular (S, n) and diffuse (s, r) material properties were estimated and the results are presented and described in this section. The minimum relative RMS error was 1.6% and the maximum relative RMS error was 7%. The average RMS error was 3.4%. The LiDAR scanner's sensor exhibits fluctuations in intensity (brightness) readings due to internal electronic noise and the pipes' surfaces are not one solid color (nonhomogeneities), in general, so deviations from the measured results are expected. Plots illustrating a cross-section of the estimated values compared to the measured values are given in Figure 5-4 – Figure 5-10. Table 5-1 presents the determined model

parameters as well as the results for the colorless specular and diffuse property estimation for each pipe. RMS_{bw} represents the error (residual) of the colorless (black and white) material estimate.

The RMS residuals of 2.7% and 2.4% for pipes 1 and 2, respectively, are reasonable due to the pipes' large radii (0.23m and 0.20m, respectively). Pipe 2 in this paper is the same as the "measured pipe" in [1]. The estimated RMS residual in [1] for this pipe was 2.88% whereas the residual estimated in this paper is lower (2.4%). The difference can be accounted for by recognizing the elimination of data on the edges of the pipe, as shown in Figure 5-2, which was not performed in [1]. Pipe 3 had a residual of 3.3%, more than double that of pipe 4, which had an RMS residual of 1.6%. When comparing the two pipes: although pipe 3 is larger, it is further away from the scanner (0.8m compared to 0.6m), which affects not only the quantity of data, but also the quality. Pipe 3 also exhibited a greater degree of nonhomogeneity in the surface color, which also contributed to the larger residual. And finally, the residual percentages were calculated based on a maximum value of 1.0, so the deviation between the estimate and the measured data will naturally be smaller for dark pipes.

Pipe 5 is a relatively far away (1.7m) cylindrical hand-rail with a radius of 0.02m (identical to pipe 4), with a painted surface that exhibits a high degree of homogeneity in the surface; thus the residual is a relatively low 2.7%. Pipes 6 and 7 were roughly the same distance from the scanner (1.5m), but varied in radius (0.03m, 0.01m, respectively). The RMS residuals of these pipes correlate with negative effect that distance and size have on the results with a 4.0% residual and 7.0% residual, respectively.

In general, the Oren Nayar general model [20] of diffuse reflectance was effective in modeling the surface properties of the pipes. The surface roughness (σ) estimated by the inversion process varied between 0.11 and 0.73 for the seven pipes. Although the inversion process was not performed using ρ alone, (setting $\sigma = 0$), without the generalized diffuse representation ($1 > \sigma > 0$), it is safe to assume that the reflectance properties of the pipes would not be estimated as accurately.

The specular reflective properties of the pipes varied significantly. Pipe 3 exhibited essentially no specular reflectance ($S = 0$) while pipes 6 and 7 demonstrated relatively high specular reflectance: $S = 0.58$ and 0.57, respectively. (A specular coefficient of $S = 1.0$ using LiDAR data signifies the object reflects and the sensor detects 100% of the incident, transmitted light). Images of the measured data and the estimated data for each pipe are shown in Figure 5-11.

The inversion process for this paper ends once the misfit changes from iteration to iteration by 1%. A more sophisticated analysis of the noise in the system based on the overall brightness of the pipe may yield a better exit criterion; however, such an investigation is beyond the scope of this paper. One can see the convergence of the two diffuse model parameters (ρ and σ) for pipe 3 in Figure 5-12.

Solid dots denote the estimate. The circle "o" denotes the final iteration after exiting (misfit = 4.30), while the hash "x" denotes the combination of values that produces the minimum norm of the residual (misfit = 4.17).

5.4.2   Ambient and Diffuse Color Properties

The ambient and diffuse color properties were estimated and the results are presented and described in this section. The complex nature of visible light, as described in Section 2.2, contributed significantly to the RMS residual of the color material properties. The mean RMS residual was 33.7 out of 255 (or 13.2%). The highest RMS error was 20.0% and the lowest was 9.1%, compared to 3.4%, 7.0%, and 1.6% for the colorless property estimates. Factors affecting the estimates include uncontrolled light sources, multiple light sources, prevalent shadows, and surface nonhomogeneities. Table 5-2 shows the estimated values for each parameter as well as the RMS residual for each pipe.

The size of the pipe had less of an effect on the results when compared to the effect the harsh shadows demonstrated. Pipe 1 is roughly the same size as pipe 2 (0.23m and 0.20m, radii, respectively), yet pipe 1 had very few shadows while pipe 2 had many harsh shadows. Pipes 4 and 6 are very dark, and roughly the same size; however, pipe 4 was 0.6m away and pipe 6 was 1.5m away, affecting both the quantity and the quality of data. Pipe 5 exhibited an RMS residual of 9.7% (nearly as low as the minimum 9.1% for pipe 4), is painted yellow, and has a relatively homogeneous surface color with very few shadows. Pipes 3 and 7 have relatively bright diffuse properties, are both rather small (0.03m and 0.01m, respectively), and thus have very similar RMS residuals of 37.6 and 38.0, respectively.

Images of the measured data and the estimated data for each pipe are shown in Figure 5-13. The colorless specular values and colorless surface roughness values determined for each pipe (Section 5.3.1) were used in conjunction with the color ambient

and diffuse values to create the images. A single point source light was manually placed for each image to approximate the complex lighting conditions seen by each pipe.

5.5 Conclusions

Specular, diffuse, and ambient material properties for seven different pipes from an industrial plant were estimated in this paper. The methods and results of this paper were divided into two sections, colorless and colored. The colorless specular and diffuse properties were measured using a LiDAR scanner. These material properties were then estimated using the numerical inversion technique outlined in [1]. The average RMS residual for the colorless properties was 3.4% while the minimum and maximum were 1.6% and 7.0%, respectively. The most significant contributor to the residual was the distance to the pipe from the scanner. Other factors include the internal noise in the LiDAR measurement system, the brightness of the pipe, and the homogeneity of the surface color. Pipes with nonhomogeneous surface colors exhibit larger RMS residuals. Furthermore, darker pipes have lower brightness values, so the RMS residuals are inherently smaller.

Color ambient and diffuse properties were measured using digital photography. Due to the complex nature of natural visible light in an industrial plant, numerical inversion was not used to estimate these parameters. Instead, k-means clustering was used to separate ambient from diffuse data, and then optimal values for each color were chosen from histogram bins. An average RMS residual of 13.2% was observed for the color data. The minimum and maximum were 9.1% and 20.3%, respectively. These residual values are much larger than those of the colorless data due to the complexity and

uncertainty of the lighting system for visible light. Harsh shadows contributed most significantly to the discrepancies. Multiple, unknown light sources also played a dominant factor. For both types of data, the distance to the scanner played a role in the accuracy.

The methods described in this paper can effectively estimate specular, diffuse, and ambient color material properties to accurately model primitives in an industrial plant. Although the techniques described herein focus on pipes, they can be applied to other primitive types. These models may be efficiently utilized in (CAD) and inspection, virtual reality training, marketing, or other visualization systems.

5.6 References

[1] Baker, B., Furse, C., "Determining Reflectance Properties of Industrial Plant Primitives," submitted to: *Geometry, Imaging and Computing*, 2013.

[2] Posada, J., "Ontology Supported Semantic Simplification of Large Data Sets of Industrial Plant CAD Models for Design Review Visualization," *Knowledge-Based Intelligent Information and Engineering Systems*, vol. 46, no. 1-2, Jan 2005.

[3] Rabbani Shah, T., "Automatic reconstruction of industrial installations using point clouds and images." Ph.D. dissertation, Dept. Elect. Eng., Delft Univ. of Tech., Delft, Netherlands.

[4] Jorge, C., et al. (2010, Aug 17) *Nuclear Plants and Emergency Virtual Simulations Based on a Low-Cost Engine Reuse. Nuclear Power*, [Online]. Available: http://www.intechopen.com/books/ nuclear-power/nuclear-plants-and-emergency-virtual-simulations-based-on-a-low-cost-engine-reuse

[5] Cook, J., "Virtual Reality for large-scale industrial applications," *Future Generation Computer Systems*, vol 14, Issue 3-4, August 1998, pp. 157-166

[6] Hubbold, R., "The Use of Virtual Reality for Training Process Plant Operatives", *Computer Graphics Expo '94 Conference*, Wembley, London, 9th November 1994.

[7]   Manocha, D. "Interactive Walkthroughs of Large Geometric Datasets," *SIGGRAPH 1999*, Los Angeles, CA, USA, 1999.

[8]   Hubbold, R., "Landmarking for navigation of large models," *Computers and Graphics*, vol. 23, no. 5, pp. 729-738, 1999.

[9]   Aliaga, D., "A Framework for the Real-time Walkthrough of Massive Models," UNC Chapel Hill, Comp. Sci. Technical Report, TR98-013, 1998.

[10]   Chapman, D., "An omnidirectional imaging system for the reverse engineering of industrial facilities," *The International Archives of the Photogrammetry, Remote Sensing and Spatial Information Sciences*, vol. 34, no. XXX, 8 pages, 2004.

[11]   Tangelder, J. W. H., "Cad-based photogrammetry for reverse engineering of industrial installation," *Computer-Aided Civil and Infrastructure Engineering*, vol. 18, no. 1, pp. 264–274, Jan 2003.

[12]   Tang, P., "Automatic reconstruction of as-built building information models from laser-scanned point clouds: A review of related techniques", *Automation in Construction*, Volume 19, Issue 7, Pages 829-843, November 2010.

[13]   Khalifa, I., "Range image segmentation using local approximation of scan lines with application to cad model acquisition," *Machine Vision Applications*, vol. 13, no.5-6, pp. 263–274, 2003.

[14]   Goulette. F. "Automatic CAD modeling of industrial pipes from range images," *Proc., Int. Conf on Recent Advances in 3- D Digital Imaging and Modeling*, Ottawa, Ontario, Canada, May 1997, pp. 229-233.

[15]   Sanders, F. H., "3D Laser Scanning Helps Chevron Revamp Platform," *Oil-and-Gas-Journal*, 2001.

[16]   Lee, J., "Skeleton-based 3D reconstruction of as-built pipelines from laser-scan data," *Automation in Construction*. vol.35, Nov 2013, pp 199–207.

[17]   Hong, J. "3D modelling of industrial piping systems using digital photogrammetry and laser scanning," M.S. Thesis, Dept. Elec. Eng., Ryerson Univ., Ottawa, Ontario, Canada, 2003.

[18]   Turkan, Y., "Automated progress tracking using 4D schedule and 3D sensing technologies," *Automation in Construction*, vol. 22, March 2012, Pages 414-421.

[19]   Mohammad R. "Adaptive vision-based crack detection using 3D scene reconstruction for condition assessment of structures," *Automation in Construction*, vol. 22, March 2012, Pages 567-576.
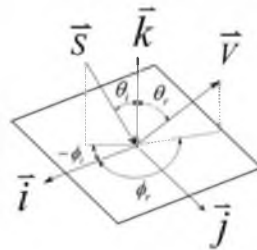
[20] Oren, M., „Generalization of the Lambertian model and implications for machine vision," *International Journal of Computer Vision*, vol. 14, no. 3, 1995, pp. 227-251.

[21] Phong, B., "Illumination for Computer Generated Pictures," *Communications of the ACM*, vol. 18, no. 6, pp. 311-317, 1975.

[22] Calabi Yau Systems. (2013, Dec 26), *LD3 Studio*, http://www.calabiyausystems.com/ Products-LD3Studio.aspx#!/page_products_ld3studio

[23] Bentley Systems Website, (2013, Dec 12), *Microstation Productline*. [Online]. http://www.bentley.com/en-US/Products/microstation+product+line/

[24] Shakarji, C. "Least-Squares Fitting Algorithms of the NIST Algorithm Testing System" *Journal of Research of the National Institute of Standards and Technology*, vol. 103, no. 6, November–December 1998, pp. 633-641.

[25] MacQueen, J. B. "Some Methods for classification and Analysis of Multivariate Observations". *Proceedings of 5th Berkeley Symposium on Mathematical Statistics and Probability*, 1. University of California Press. 1967, pp. 281–297.

[26] Roh, S., "Visualization Application for Interior Progress Monitoring. 3D Environment", *Construction Research Congress (CRC)*, Seattle, Washington, April 5-7, 2009.

Table 5-1: Results of Colorless Specular and Diffuse Parameter Estimation

pipe #	dist(m)	radius (m)	S	n	ρ_{bw}	σ	RMS_{bw}	ρ_{bw}
1	0.7	0.23	0.04	32.89	0.47	0.30	0.027	
2	1.9	0.20	0.15	41.21	0.50	0.22	0.024	
3	0.8	0.03	0.00	14.19	0.66	0.39	0.033	
4	0.6	0.02	0.10	47.82	0.24	0.45	0.016	
5	1.7	0.02	0.28	59.21	0.45	0.11	0.027	
6	1.5	0.03	0.58	148.26	0.28	0.73	0.040	
7	1.5	0.01	0.57	44.07	0.24	0.19	0.070	

Table 5-2: Results of Ambient and Diffuse Color Estimation

pipe #	radius (m)	α_r	α_g	α_b	ρ_r	ρ_g	ρ_b	rms_{rgb}	α_{rgb}	ρ_{rgb}
1	0.23	75	88	95	98	95	106	23.2		
2	0.20	82	103	111	72	64	90	51.7		
3	0.03	170	167	157	41	44	49	37.6		
4	0.02	52	54	52	52	54	52	20.0		
5	0.02	188	162	26	41	39	28	24.7		
6	0.03	54	59	59	54	59	59	40.9		
7	0.01	103	67	41	103	80	95	38.0		

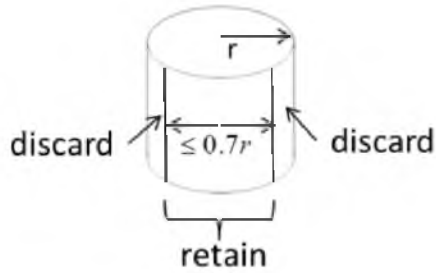**Figure 5-1: Geometric representation for Oren Nayar diffuse model**

Figure 5-2: Geometric representation of regions of nonlinear data that were discarded
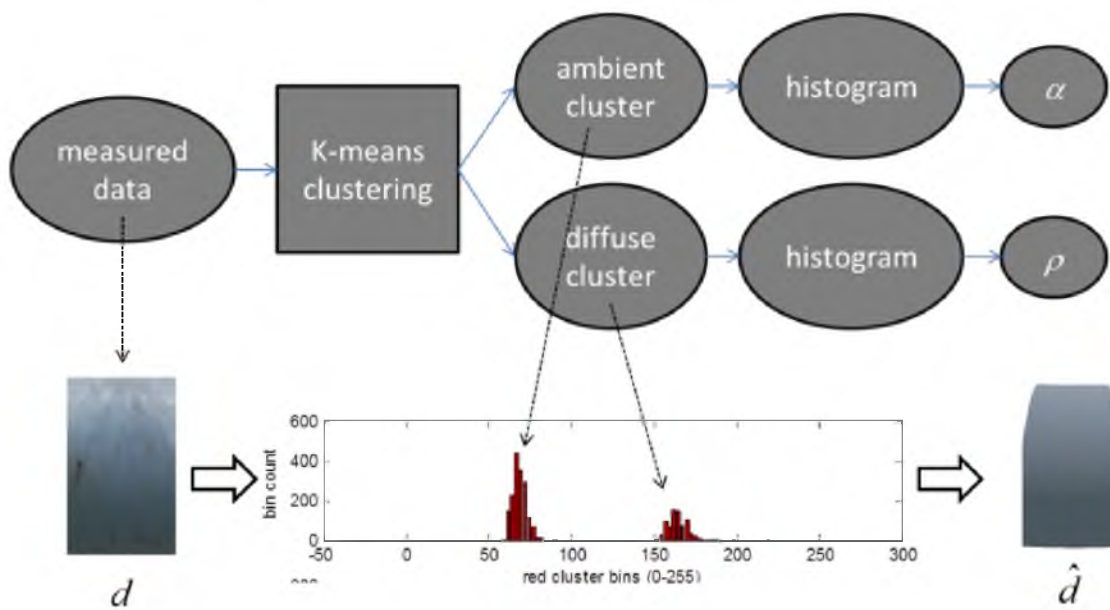

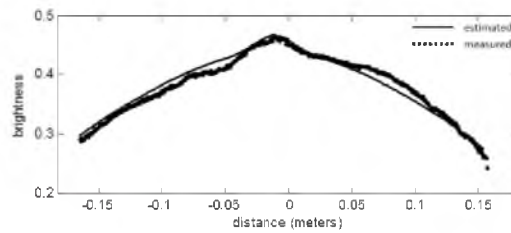**Figure 5-3: Flowchart of the k-means clustering algorithm**
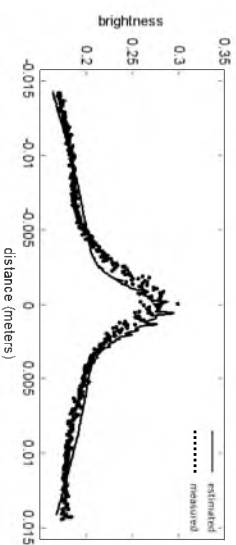

Figure 5-4: Estimated vs. measured data for pipe 1

Figure 5-7: Estimated vs. measured data for pipe 4
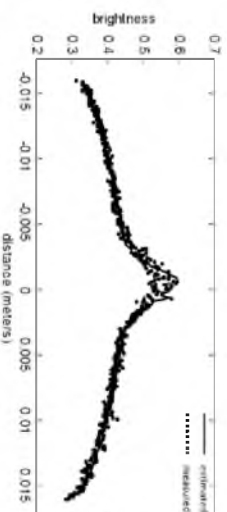

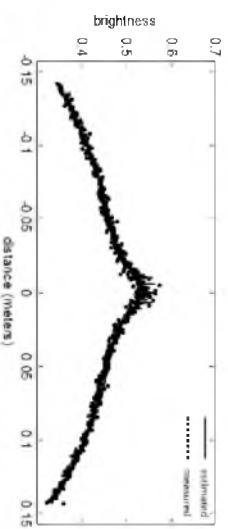**Figure 5:8: Estimated vs. measured data for pipe 5**
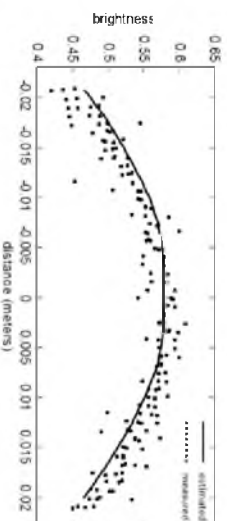
Figure 5-5: Estimated vs. measured data for pipe 2

Figure 5-6: Estimated vs. measured data for pipe 3
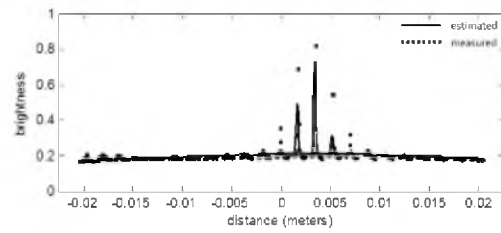
Figure 5-9: Estimated vs. measured data for pipe 6
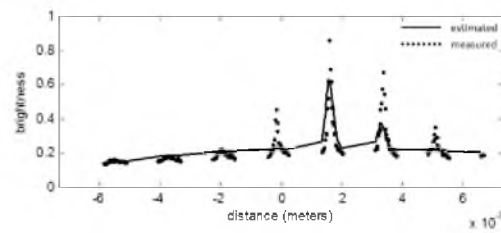
Figure 5-10: Estimated vs. measured data for pipe 7

Figure 5-11: Estimated vs. measured colorless (LiDAR) data for all pipes

Figure 5-12: Convergence of the diffuse parameters for pipe 3

Figure 5-13: Measured and estimated experimental results for colored pipes. Pipes 4 and 5 appear to be leaning slightly in the estimated data, but not in the measured data. The pipes are actually leaning, but the image used for this figure occupies a rectangle.

CHAPTER 6

CONCLUSION AND FUTURE WORK

6.1   Contributions

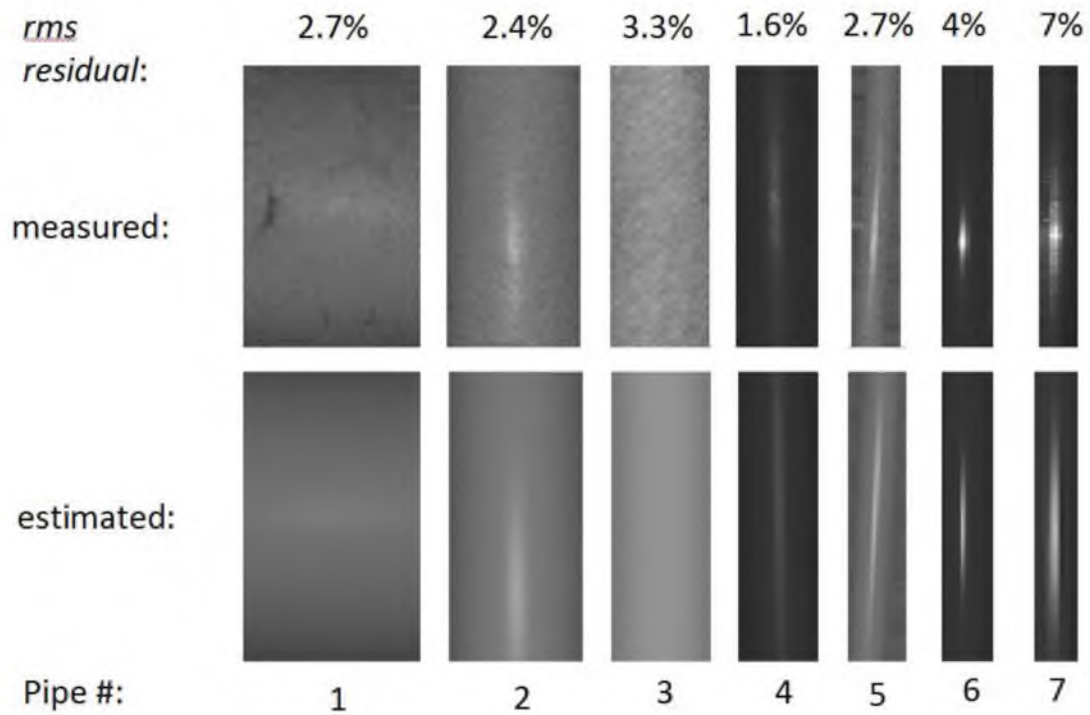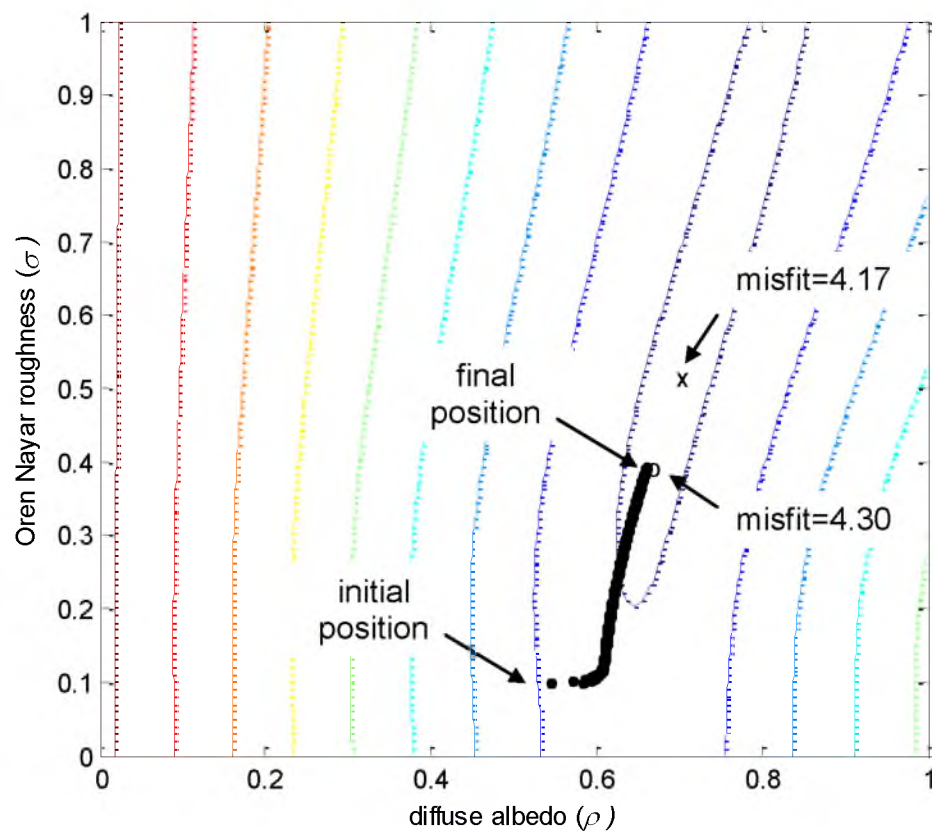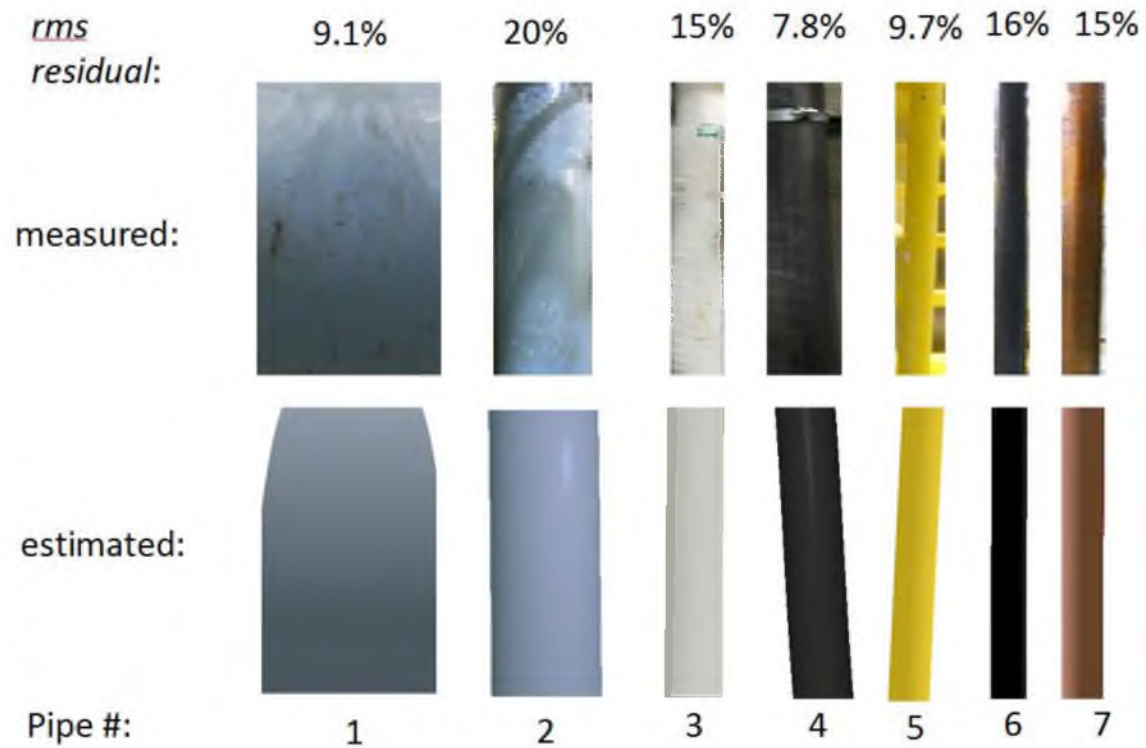The purpose of this research was to offer an efficient alternative to point clouds or texture mapping to achieve near photorealistic rendering with minimal storage for 3D models of industrial plant primitives. First, an analysis of errors associated with creating 3D model geometry from LiDAR data was presented. In order to estimate reflectance material properties, geometric models of pipes were then created manually from LiDAR data. Colorless specular and diffuse material properties were estimated using LiDAR intensity data. Finally, colored ambient and diffuse material properties were determined and combined with the colorless specular and diffuse materials to create corresponding 3D models.

6.1.1   3D Modeling Error Analysis

An error analysis of polygonal models created from actual and modeled terrestrial LIDAR data was performed. Ray traced points were compared to actual LIDAR scan data and modeled data using Fourier spectra, Taylor expansion, and statistics. The standard deviation of error for the polygonal model of the anomalous groove was 0.474mm; the error for the bump was 0.599mm; and the error for the incline was 0.008mm.

This analysis showed that for objects with few high frequency features, scanning at a higher density actually increases measurement error. Polygonal models can act as filters to remove high frequency noise, thus lowering the errors inherent in LIDAR data utilization. Polygonal models created from LIDAR scan data can thereby be used to accurately represent real-world objects. Furthermore, due to the error inherent in LIDAR scanning hardware, polygonal models can actually yield lower standard deviations of error than LIDAR scanning at a higher resolution.

6.1.2   Colorless Specular and Diffuse Estimation

A method for determining the specular and diffuse reflectance properties for two ideal and one measured pipe from an industrial plant was presented. LiDAR data intensity values provided the brightness data for the measured cylinder. The reflectance properties determined include the specular coefficient and specular exponent commonly used in computer graphics, as well as the diffuse albedo parameter and the Oren-Nayar roughness parameter.

Newton's method from numerical inversion was used to compute the estimate for the model parameters. The inversion process for the ideal cylinders recovered the model parameters within 3.6% of the actual values, providing a suitable method for recovering reflectance parameters.

Inversion of the model parameters for the measured cylinder provided an accurate estimate to the actual data to within 3.5% for all brightness values over 0.3. The relative errors associated with brightness estimation for data at the extreme edges of the pipe,

where the incident angle is close to orthogonal to the surfaced normal, were as high as 44.7% due to nonlinear amplifiers in the detection hardware.

6.1.3 Color Ambient and Diffuse Estimation

Specular, diffuse, and ambient material properties for seven different pipes from an industrial plant were estimated in this paper. The methods and results of this paper were divided into two sections, colorless and colored. The colorless specular and diffuse properties were measured using a LiDAR scanner. These material properties were then estimated using the numerical inversion technique outlined in [1]. The average RMS residual for the colorless properties was 3.4% while the minimum and maximum were 1.6% and 7.0%, respectively. The most significant contributor to the residual was the distance to the pipe from the scanner. Other factors include the internal noise in the LiDAR measurement system, the brightness of the pipe, and the homogeneity of the surface color. Pipes with nonhomogeneous surface colors exhibit larger RMS residuals. Furthermore, darker pipes have lower brightness values, so the RMS residuals are inherently smaller. Table 6-1 shows the results for each of the seven pipes.

A visual depiction of the experimental results for the colorless specular and diffuse parameters is given in Figure 6-1. On some of the darker pipes, the specular spread seems to exceed that of the measured pipes. This is most likely due to the sensitive nature of the specular parameter. The specular component only affects a small portion of the overall data, and therefore, its contribution to the misfit is hidden by the noise in the system.

The numerical inversion technique used to estimate the colorless material properties was the steepest descent algorithm. The model parameter convergence is illustrated in Figure 6-2. The diffuse albedo (ρ) is on the horizontal axis and the Oren Nayar surface roughness (σ) is on the vertical axis. The exit criterion for the iterative process is when the relative change in the misfit is less than 1%. The misfit at the end of the process for this pipe (pipe number 3) was 4.30 and an array of misfit values was computed for this pipe, and the overall minimum was found to be 4.17. One may observe from this that the exit criterion could possibly be improved to achieve a better approximation to the model parameters that yield the minimum misfit.

Color ambient and diffuse properties were measured using digital photography. Due to the complex nature of natural visible light in an industrial plant, numerical inversion was not used to estimate these parameters. Instead, k-means clustering was used to separate ambient from diffuse data, and then optimal values for each color were chosen from histogram bins. Table 6-2 shows the results for the seven pipes analyzed.

An average RMS residual of 13.2% was observed for the color data. The minimum and maximum were 9.1% and 20.3%, respectively. These residual values are much larger than those of the colorless data due to the complexity and uncertainty of the lighting system for visible light. Harsh shadows contributed most significantly to the discrepancies. Multiple, unknown light sources also played a dominant factor. For both types of data, the distance to the scanner played a role in the accuracy. Figure 6-3 illustrates the measured data and the estimated data, and shows the root mean square residual associated with each pipe. The measured data shown are rectangular regions extracted from the original color image. In some instances (namely pipes 4 and 5) the

pipe is oriented at an angle, which is reflected in the estimated image (no color information is estimated beyond the radius of the pipe). In the measured data, the regions surrounding the pipe may appear in the image, but were not used in the estimation of the color material properties for those pipes. To see the slightly slanted pipes in the original image, refer to Figure 1-1 and Figure 1-2.

In spite of these challenges, the methods described in this paper estimate specular, diffuse, and ambient color material properties to accurately model primitives in an industrial plant. This research offers an efficient alternative to rendering point clouds or texture mapped polygons to achieve near photorealistic rendering with minimal storage for 3D models of industrial plant primitives. Alternatives such as colored point clouds may be rendered in real-time; however, the visual quality is usually poor due to the lack of data between points. Furthermore, direct CAD work on point clouds is difficult due to the disparate nature of the data. Textured polygons can provide a rich viewing experience, but at a high cost of computational complexity, high texture memory bandwidth, and massive data storage. Additionally, textures are static elements of the model; without material properties, real-time lighting interaction is not possible.

Models created with the material properties discovered by this research may be efficiently utilized in (CAD) and inspection, virtual reality training, marketing, or other visualization systems. The storage requirements of the material properties estimated in this project for hard drive, RAM, and texture memory are minimal when compared to alternative methods. The computational complexity of a rendering system required to display objects with material properties instead of point clouds or textured models is significantly less. Dynamic lighting with the model is especially useful when doing

marketing walk-throughs or virtual reality training, and is not possible with mere points or textures.

The methods in this project provide automated ways to contrive and utilize material properties from industrial plant primitives. These material properties can be used for visualization, object recognition, asset management, and improved computer storage and computational efficiency when compared with other methods.

6.2   Future Work

Many aspects of the research in this project can be investigated further. Some possibilities may include a performance evaluation, enhancements to the numerical inversion process, application to a broader type of industrial plant or other object, and object recognition.

An evaluation of the performance enhancement obtained by utilizing reflectance material properties obtained in this project instead of texture maps in a rendering system could be enlisted. Metrics such as hard drive storage capacity, texture memory utilization, rendering frame rate, or other could be compared. An alternate comparison study could also include a listing of CAD or other visualization or design tools that would support the rendering of the material properties that were determined in this project. Such systems' relative performance could also be measured and compared.

The numerical inversion process could be improved in a few ways. For one, the exit criterion for the steepest descent algorithm was based on the misfit changing by less than 1% from iteration to iteration. A more sophisticated criterion could be established if the relative noise levels for various pipe intensities, so that the inversion process

converges to a more accurate result. Secondly, an alternate algorithm such as the stochastic or conjugate gradient or a regularized Newton method may be employed for at least an order of magnitude better (faster) convergence [2], [3]. The steepest descent algorithm was chosen due to its ease of implementation and comprehension. Now that the concept of utilizing numerical inversion to determine material properties has been demonstrated, a more powerful method may be employed. The stochastic gradient method is simple to implement, but can be somewhat more complicated to conceptualize. Newton's method may demonstrate instabilities due to the inversion of a matrix that may be ill conditioned, so a regularized method is advisable. Such a solution requires more investment in the implementation phase, but the convergence is the best of the three methods. Thirdly, the model chosen to represent the material properties was assumed to be homogeneous. This greatly simplified the numerical inversion, but may not be the most accurate. If the model parameters of the inversion varied along the length of a pipe, material properties of a nonhomogeneous surface could be detected. This would require additional terms in the model parameter vector used in the inversion process.

Alternately, if the specular and diffuse reflectance values of the industrial plant primitives in their current state were known, the material type could be automatically estimated. Furthermore, the annotation data such as density, melting point, specific heat, life expectancy, or even the inner diameter could be automatically estimated (when utilized in conjunction with geometric information such as a cylinder's outer radius) once the object has been identified with a matching material type in a database library. Statistical data could be acquired, analyzed, and archived in a database to which future results could be compared. Such an exercise could be effective in automatically

determining the object's material type (such as wood, painted surface, stainless steel, vinyl, ceramic, or other).

Oren and Nayar [4] provided the generalized model for the diffuse reflectance, but few systems can readily render the surface roughness component in real-time. Additional work could reveal a high-efficiency alternative to the Oren Nayar model so more rendering systems could illustrate the generalized diffuse properties more efficiently in real-time.

Finally, the results in this paper need not be confined to pipe primitives, or even an industrial plant. There are many objects that demonstrate reflective properties that would be interesting to study. Research fields such as geology, studying material properties of the moon, or historical preservation are a few of the areas to which these methods could be applied.

6.3   References

[1]   Baker, B., Furse, C., "Determining Reflectance Properties of Industrial Plant Primitives," submitted to: *Geometry, Imaging and Computing,* 2013.

[2]   Tarantola, A. *Inverse Problem Theory and Methods for Model Parameter Estimation.* Philadelphia, PA: SIAM, 2005.

[3]   Zhdanov, M., *Geophysical Inverse Theory and Regularization Problems.* New York, NY: Elsevier Science, 2002.

[4]   Oren, M., „Generalization of the Lambertian model and implications for machine vision," *International Journal of Computer Vision,* vol. 14, no. 3, 1995, pp. 227-251.

Table 6-1: Colorless Diffuse Parameter Results

pipe #	dist(m)	radius (m)	S	n	ρ_{bw}	σ	RMS_{bw}	ρ_{bw}
1	0.7	0.23	0.04	32.89	0.47	0.30	0.027	
2	1.9	0.20	0.15	41.21	0.50	0.22	0.024	
3	0.8	0.03	0.00	14.19	0.66	0.39	0.033	
4	0.6	0.02	0.10	47.82	0.24	0.45	0.016	
5	1.7	0.02	0.28	59.21	0.45	0.11	0.027	
6	1.5	0.03	0.58	148.26	0.28	0.73	0.040	
7	1.5	0.01	0.57	44.07	0.24	0.19	0.070	

Table 6-2: Colored Diffuse Parameter Results

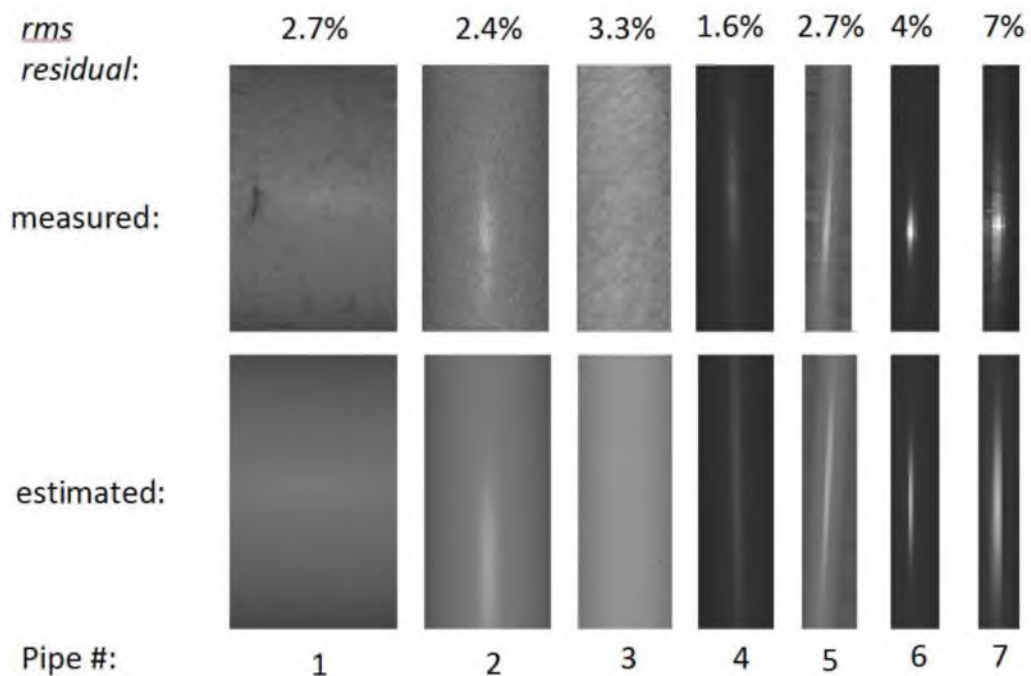| pipe #	radius (m)	α_r	α_g	α_b	ρ_r	ρ_g	ρ_b	rms_{rgb}	α_{rgb}	ρ_{rgb}
1	0.23	75	88	95	98	95	106	23.2		
2	0.20	82	103	111	72	64	90	51.7		
3	0.03	170	167	157	41	44	49	37.6		
4	0.02	52	54	52	52	54	52	20.0		
5	0.02	188	162	26	41	39	28	24.7		
6	0.03	54	59	59	54	59	59	40.9		
7	0.01	103	67	41	103	80	95	38.0		

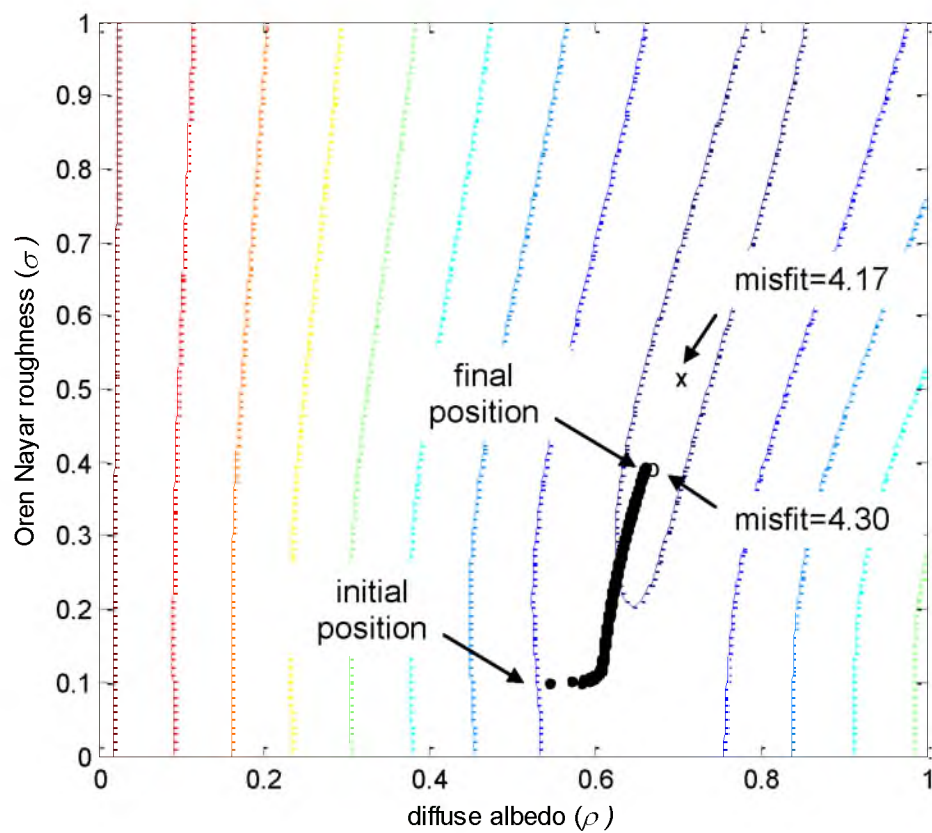**Figure 6-1: Measured and estimated results for specular and diffuse material estimation**

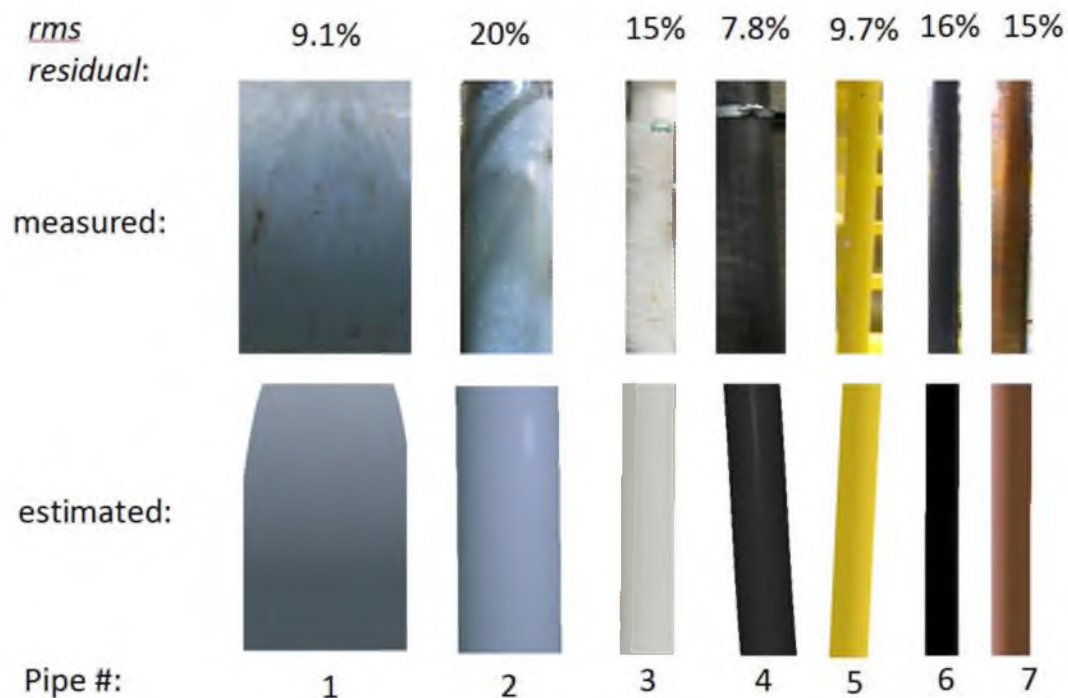**Figure 6-2: Misfit tracking for roughness and albedo model parameters**

Figure 6-3: Measured and estimated experimental results for colored pipes. Pipes 4 and 5 appear to be leaning slightly in the estimated data, but not in the measured data. The pipes are actually leaning, but the image used for this figure occupies a rectangle